AGU Advances

First Revision [Accepted] of

Very low frequency earthquakes in between the seismogenic and tremor zones in Cascadia?

Wenyuan Fan[1], Andrew J. Barbour[2], Jeffrey J. McGuire[2], Yihe Huang[3], Guoqing Lin[4], Elizabeth S. Cochran[5], & Ryo Okuwaki[6]

[1] Scripps Institution of Oceanography, UC San Diego, La Jolla, California, USA
[2] U.S. Geological Survey, Earthquake Science Center, Moffett Field, California, USA
[3] Department of Earth and Environmental Sciences, University of Michigan, Ann Arbor, Michigan, USA
[4] Rosenstiel School of Marine and Atmospheric Science, University of Miami, Miami, Florida, USA
[5] U.S. Geological Survey, Earthquake Science Center, Pasadena, California, USA
[6] Mountain Science Center, Faculty of Life and Environmental Sciences, University of Tsukuba, Tsukuba, Ibaraki, Japan

Very low frequency earthquakes in between the seismogenic and tremor zones in Cascadia?

Wenyuan Fan[1], Andrew J. Barbour[2], Jeffrey J. McGuire[2], Yihe Huang[3], Guoqing Lin[4], Elizabeth S. Cochran[5], & Ryo Okuwaki[6]

[1]Scripps Institution of Oceanography, UC San Diego, La Jolla, California, USA
[2]U.S. Geological Survey, Earthquake Science Center, Moffett Field, California, USA
[3]Department of Earth and Environmental Sciences, University of Michigan, Ann Arbor, Michigan, USA
[4]Rosenstiel School of Marine and Atmospheric Science, University of Miami, Miami, Florida, USA
[5]U.S. Geological Survey, Earthquake Science Center, Pasadena, California, USA
[6]Mountain Science Center, Faculty of Life and Environmental Sciences, University of Tsukuba, Tsukuba, Ibaraki, Japan

Key Points:

- Three large VLFEs in Cascadia were dynamically triggered by teleseismic waves.
- These VLFEs likely occurred in between the seismogenic and tremor zones.
- One VLFE has a moment magnitude of 5.7, the largest VLFE detected to date and the first detected geodetically.

Corresponding author: Wenyuan Fan, wenyuanfan@ucsd.edu

Abstract

Megathrust earthquakes and their associated tsunamis cause some of the worst natural disasters. In addition to earthquakes, a wide range of slip behaviors are present at subduction zones, including slow earthquakes that span multiple orders of spatial and temporal scales. Understanding these events may shed light on the stress or strength conditions of the megathrust fault. Out of all types of slow earthquakes, very low frequency earthquakes (VLFEs) are most enigmatic because they are difficult to detect reliably, and the physical nature of VLFEs are poorly understood. Here we show three VLFEs in Cascadia that were dynamically triggered by a 2009 Mw 6.9 Canal de Ballenas earthquake in the Gulf of California. The VLFEs likely locate in between the seismogenic zone and the Cascadia episodic tremor and slip zone, including one event with a moment magnitude of 5.7. This is the largest VLFE reported to date, causing clear geodetic signals. Our results show that the Cascadia megathrust fault might slip rapidly at some spots in this gap zone, and such a permissible slip behavior has direct seismic hazard implications for coastal communities and perhaps further inland. Further, the observed seismic sources may represent a new class of slip events, whose characteristics do not fit current understandings of slow or regular earthquakes.

Plain Language Summary

Megathrust earthquakes and their associated tsunamis pose significant hazards in Cascadia. In addition to earthquakes, episodic tremor and slip events have been discovered in the region at depths of 30 to 50 km, 10–15 km below the seismogenic zone. The expected slip behavior between the seismogenic and tremor zones remains unknown, leaving the rupture extents of future megathrust earthquakes unclear. We detect and locate three very low frequency earthquakes near this gap region, including one with a moment magnitude of 5.7. This is the largest very low frequency earthquake reported to date, and its detection not only shows that the fault slip behaviors in this gap zone can be highly heterogeneous but also challenges current understanding of slow earthquake physics.

1 Introduction

The Cascadia subduction zone poses serious earthquake and tsunami hazards to some of the most populous regions of the United States and Canada. Geological records reveal that at least 19 great megathrust earthquakes occurred in the region over the past ten thousand years [*Walton et al.*, 2021]. However, as an exceptionally seismically quiet subduction zone [*Wang and Tréhu*, 2016], large megathrust earthquakes in Cascadia have never been recorded by modern instrumentation. In contrast, slow earthquakes, which differ from regular earthquakes in their seismic radiations and rupture speeds, occur frequently across the whole subduction zone [*Brudzinski and Allen*, 2007; *Gomberg et al.*, 2010]. These slow earthquakes encompass a wide spectrum of slip behaviors [*Peng and Gomberg*, 2010], including slow slip events (SSEs) [*Dragert et al.*, 2001], very low frequency earthquakes (VLFEs) [*Ghosh et al.*, 2015; *Hutchison and Ghosh*, 2016], low-frequency earthquakes [*Brown et al.*, 2009; *Bostock et al.*, 2012; *Sweet et al.*, 2019], and non-volcanic tremor [*Wech and Creager*, 2008]. In Cascadia, slow slip and non-volcanic tremor often occur concurrently with each other as episodic tremor and slip (ETS) events [*Rogers and Dragert*, 2003; *Bartlow et al.*, 2011].

These ETS events recur semi-regularly every 11 to 15 months and can propagate unilaterally or bilaterally [*Dragert and Wang*, 2011; *Wech and Bartlow*, 2014]. They can have moment magnitudes equivalent to Mw 6.7 earthquakes with the SSEs releasing most of their moments [*Dragert et al.*, 2001; *Kao et al.*, 2010]. These events accommodate a portion of the slip deficit at the subduction zone and concentrate along a band at depths of 30–50 km, about 10 to 15 km deeper than the downdip edge of the seismogenic zone [*Brudzinski and Allen*, 2007; *Gomberg et al.*, 2010; *Wang and Tréhu*, 2016; *Walton et al.*, 2021]. Additionally, typical VLFEs in the region can have equivalent moment magnitudes ranging from 2.1 to 4.1 [*Ghosh et al.*, 2015; *Hutchison and Ghosh*, 2016; *Ide*, 2016]. In between the tremor

zone and the seismogenic zone on the fault, there is a gap that is not fully locked, yet devoid of slow earthquakes [*Hyndman and Wang*, 1995; *Wang et al.*, 2003; *Brudzinski and Allen*, 2007; *Gomberg et al.*, 2010; *Priest et al.*, 2010; *Schmalzle et al.*, 2014]. Understanding the slip behaviors in this gap zone gives insight into the stress and strength conditions of the megathrust fault, and can lead to improved forecasting of future earthquake rupture scenarios [*Bruhat and Segall*, 2016; *Ramos and Huang*, 2019]. Studies of this gap zone are largely hindered by a lack of robust observations, or the loss of resolution of onshore instruments; hence, little is known about the nature of the gap zone or its relation to the locked zone and the tremor zone.

VLFEs differ from tremor and regular earthquakes with similar magnitudes as they are rich in low-frequency radiation content in a band of ~20–50 seconds and depleted in high-frequency radiation ($\geq$ 1 Hz) [*Obara and Ito*, 2005; *Ito and Obara*, 2006; *Ito et al.*, 2007]. Their apparent correlations with ETS events in Cascadia seem to indicate that VLFEs are another seismic manifestation of slow slip, similar to tremor and low frequency earthquakes but responsible for a larger portion of the moment release [e.g., *Ghosh et al.*, 2015]. However, the relationship between VLFEs and SSEs are more complicated than those between tremor and SSEs [e.g., *Bartlow et al.*, 2011]. For example, VLFEs in Cascadia can correlate with ETS events either spatiotemporally [*Ghosh et al.*, 2015] or only temporally [*Hutchison and Ghosh*, 2016]. In either case, previously identified VLFEs in Cascadia were all located in the tremor zone at depths of 30–50 km, and they are almost always accompanied by tremor [*Ghosh et al.*, 2015; *Hutchison and Ghosh*, 2016; *Ide*, 2016].

In a search of the USArray seismic data from August to October 2009 (see Open Research), we find that three VLFEs occurred over a 5-minute period. Two of the VLFEs likely occurred in the gap zone between the seismogenic locked zone and the tremor zone, and one is likely adjacent to the gap zone (Figure 1). Geodetic data confirm the best resolved event, with clear observations of static strains that are consistent with the seismically derived focal mechanism. The VLFEs coincide with surface wave arrivals of the August 2009 Mw 6.9 Canal de Ballenas earthquake in the Gulf of California, Mexico, and we examine whether the VLFEs may have been triggered by the dynamic stresses from the passing waves. These events were also close to the onset area of the 2009 Cascadia ETS event and occur three days before its reported initiation [*Bartlow et al.*, 2011]. This spatiotemporal correlation between the VLFEs and ETS event suggests that these previously unknown VLFEs were either diagnostic of, or played a role in, the nucleation process of the 2009 Cascadia ETS event. Most importantly, identifying these VLFEs offers new insight into the physical nature of the gap zone.

2 Datasets and Methods

2.1 Detecting and Locating VLFEs in Cascadia

We use an array-based surface wave detector that is developed from the AELUMA method (Automated Event Location Using a Mesh of Arrays) [*de Groot-Hedlin and Hedlin*, 2015; *Fan et al.*, 2018]. The method takes advantage of local coherence of the recorded signals, and then forms an inverse problem to locate the signal sources assuming that the waves propagate along great circle paths [*de Groot-Hedlin and Hedlin*, 2015; *Fan et al.*, 2018]. Here we follow the same data processing protocol outlined in *Fan et al.* [2018] and use the same empirical parameters that have been implemented to investigate stormquakes and submarine landslides in the Gulf of Mexico [*Fan et al.*, 2019, 2020]. The only difference is that we use 360 s time-window and 180 s time-step for the beamforming procedure instead of using the 600 s time-window and 300 s time-step as used in previous studies.

We first divide the large arrays into small subarrays, each comprising three stations. Second, tau-p beamforming analysis is applied to continuous data that are filtered in the 20 to 50 s period band to detect signals, and the detections are screened through a quality control

procedure, such as examining cross-correlation coefficient, phase velocity, and beam-power value of each detection [see details in *Fan et al.*, 2018]. The records (LHZ component) are downloaded from available stations in the contiguous United States during the study period (see Open Research). We use vertical records because Rayleigh waves are used to detect the seismic sources, and vertical components generally have lower noise levels compared to horizontal components. Due to the signal to noise ratios and the quality control steps, not all records are used for the final location. Third, the remaining detections are grouped into non-overlapping clusters. Fourth, detections of each cluster are used to locate one seismic source and its location uncertainty is empirically estimated [*Fan et al.*, 2019, 2020]. During the location step, possible arrival angle anomalies are empirically corrected using earthquakes reported in the Global Centroid Moment Tensor Project [*Ekström et al.*, 2012]. Finally, the quality of each located seismic event is assessed to avoid duplicates and a catalog is populated with the located events. Our approach is data-driven with few assumptions about the nature of the seismic sources. The AELUMA method is particularly well-suited for detecting unconventional seismic sources that are commonly missed in standard catalogs [*Fan et al.*, 2019, 2020]. This is because the method applies to continuous waveforms and can detect and locate any source of seismic radiation without phase picks or knowing the source types [*Fan et al.*, 2018].

We detected three seismic sources (E1, E2, and E3) in Cascadia within 15 minutes after the 2009 Canal de Ballenas earthquake in the Gulf of California, Mexico that are likely VLFEs (Figures 1,2). Due to the temporal correlation between the earthquake surface wave arrivals and the detected sources, we hypothesize that the detected sources were triggered by the 2009 earthquake. We will discuss this hypothesis in later sections. These three VLFEs were detected by 84, 57, and 187 subarrays, respectively. The larger temporal separation between E3 and the 2009 earthquake likely allows for more detections of E3. Consequentially, E3 can be clearly seen in the record section when the traces are aligned with respect to its location (Figure 3). The location uncertainties for all three VLFEs are shown as the dashed lines in Figure 1. The location uncertainty of the detected seismic sources are computed by examining the spatial structure of a suite of grids within a misfit threshold [*Fan et al.*, 2018]. Based on the obtained location, grids that can minimize the misfit values within 25% of the minimum value are taken as possible source locations [*Fan et al.*, 2018]. From the set of possible sources, we compute a distance covariance matrix and use its eigenvectors and eigenvalues to define an uncertainty ellipse around the source location solution [*Fan et al.*, 2018] (Figure 2). This approach can provide a formal way to address statistical location uncertainty due to data availability. However, the misfit threshold is chosen subjectively. In our case, the 25% of the optimal value is a conservative choice, and the results represent the lower-bound of the resolution. In later parts, we will evaluate the event locations with local strainmeter records to provide independent constraints on the results.

2.2 Determining Focal Mechanisms of the VLFEs

We use a cross-correlation method to estimate the focal mechanisms (Figure 4). The approach shares similarities with the grid-search centroid moment tensor inversion method, which has been applied to search VLFEs in Cascadia and offshore Japan [e.g., *Ito and Obara*, 2006; *Ghosh et al.*, 2015]. The near-field stations in the Pacific Northwest (inset, Figure 1) are not used to analyze E3 due to the interference between its surface waves and those of the Canal de Ballenas earthquake (Figure S1).

Our method resolves the event focal mechanism, duration, and the event depth based on a VLFE catalog (Figure 4). Instead of searching the possible combinations of the fault geometry (strike, rake, dip) and event depth, we fix the E3 epicenter as the resolved location from our surface wave detector and use a VLFE catalog of events beneath southern Vancouver Island and northern Washington State [*Ide*, 2016] to forward calculate synthetic seismograms. Based on the amplitudes of the VLFE-related waves, we initially assume the event has a seismic moment of $2 \times 10^{18}\,\mathrm{N \cdot m}$. The catalog has 112 events, and for each focal mecha-

nism (Figure 4), we compute three-component synthetic waveforms for sources at depth from 5 km to 50 km with a 5 km increment. We also investigate a set of source durations assuming a Gaussian function shape with the duration as 6 times the standard deviation; we test durations from 0.9 s to 257.1 s.

The synthetic waveforms are computed for each station in the vertical, north-south, and east-west directions up to 3600 s with the Instaseis method [*Driel et al.*, 2015]. The Instaseis method pre-computes a Green's function database with the axisymmetric spectral-element method AxiSEM [*Nissen-Meyer et al.*, 2014]. Here, we use the Green's functions calculated with the anisotropic version of the PREM model up to 5 s [*Dziewonski and Anderson*, 1981]. These synthetic seismograms are then filtered at 25 to 50 s period band and are cross-correlated with the observed three-component waveforms (e.g., 300 s waveform outlined by the yellow band in Figure 3) of the best-resolved event, E3, in the same frequency band. We focus on stations east of the source with epicentral distances from 500 km to 3300 km (up to 30° epicentral distance, Figure 5). For each station, a representative cross-correlation coefficient is taken as the geometric mean of the cross-correlation coefficients of the three components (e.g., Figure 5), the preferred depth for the focal mechanism maximizes the total summation of the representative cross-correlation coefficients from all stations. The optimal solution, including both the focal mechanism and the event depth, has the maximum total summation of cross-correlation coefficients. After obtaining an optimal solution, we calculate the amplitude ratios between the synthetic waveforms and the observations for all the stations and components (Figure 4d), and the median value of the ratio distribution (0.25 for E3) is used to scale the initial seismic moment to compute the VLFE moment.

Given the noise level of the records, we can only estimate the focal mechanism for one of the detected seismic sources in Cascadia (E3), which has waveforms that are separated from the surface waves of the Canal de Ballenas earthquake (Figure 3). It is challenging to analyze events E1 and E2 in more detail because the high amplitude coda waves from the Canal de Ballenas earthquake mask the VLFE signal (Figure 3).

2.3 Dynamic and Static Deformation

With our starting estimates that seismic moments of the VLFEs are on the order of 10^{18} N · m, geodetic methods may detect the associated static deformation and verify our results. We use strainmeters because they are generally sensitive to static strains from small-to-moderate crustal earthquakes, and can give precise onset timing of the static deformation, unlike with more commonly used space geodetic techniques (i.e., GNSS, InSAR). They can also measure broadband dynamic strains from the Canal de Ballenas event, which allows us to robustly estimate dynamic stresses at the times of the detected seismic sources. We will later examine the relations between the dynamic stress and the observed VLFEs.

In particular, we use strain data from borehole strainmeters (BSMs) in the Network of the Americas (NOTA) (Figure 6a). These BSMs are four-component Gladwin-type differential capacitance strainmeters [*Gladwin*, 1984]. Unprocessed data given in capacitance bridge counts are converted to linear strains using standard linearization procedure [*Barbour and Crowell*, 2017]. We outline the steps taken to analyze both dynamic strains from the source, and static strains from the VLFEs.

2.3.1 Dynamic Strains from the Canal de Ballenas Earthquake

The 2009 Mw 6.9 Canal de Ballenas earthquake was a strike-slip event in the north-central region of the Gulf of California, Mexico [*Castro et al.*, 2011]. The earthquake ruptured a segment of an *en echelon* transform fault system with a shallow hypocenter close to the seafloor [*Castro et al.*, 2011; *Plattner et al.*, 2015]. The Canal de Ballenas earthquake generated strong Rayleigh waves, and the observed dynamic strains at NOTA stations were

between 2.1 and 15.3 (mean 7.3) times larger than those of most Mw 6.9 teleseisms, according to the relations of *Agnew and Wyatt* [2014].

For analyses of the teleseismic waves, we use the root-mean-square strain timeseries ϵ for the given time window, given by $\epsilon = \sqrt{\left(\sum_{i=1}^{n} g_i^2\right)/n}$, where g_i are the linear strain timeseries for the n strain channels; for these BSMs, $n = 4$ under normal operating conditions. We then calculate the peak value of the RMS strain timeseries, $\hat{\epsilon}$, after applying a two-pass Butterworth highpass filter with a corner frequency of 0.004 Hz (250 s period) to mask out all non-seismic signals that strainmeters have well-known sensitivies to (e.g., tides, atmospheric pressure, etc.); this is the peak dynamic strain (PDS).

Following *Hill* [2008], we estimate peak dynamic stress ($\hat{s}$) as the observed PDS scaled by twice the crustal shear modulus μ ($\hat{s} = 2\mu\hat{\epsilon}$). We use $\mu = 30 \times 10^9$ Pa to be consistent with the crustal velocity and density model used to locate the VLFEs. This is a simplistic estimate of the true stress perturbation, which might be larger if the event occurred where material properties contrast strongly; however, at Cascadia, contrasts in S-wave velocity (V_S) at the slab interface are generally within a few percent [*Porritt et al.*, 2011], which translates to a smaller perturbation in μ, given that $\mu = \rho V_S^2$, where ρ is density.

2.3.2 Static Strains from the Local VLFEs

Theoretically, the lowest detectable static strain is about 0.1–0.2 $\times 10^{-9}$ [parts-per-billion (ppb), or nanostrain]. Following *Wyatt* [1988] this implies that strain from an event with 10^{18} N · m seismic moment will be undetectable beyond a few hundred kilometers. However, because of noise and other unrelated signals, the practical limit of detection of an event of this size is ~100–130 km. Relative to the location of VLFE event E3, this limitation leaves 14 possible NOTA stations. However, data from four of these stations are either unavailable or too contaminated with non-seismic signals such that only stations B003, B004, B014, B007, B001, B013, B009, B010, B011, and B926 are useful for analyzing static strains (Figure 7).

The distances from these stations to VLFE event E3 range from 34 to 116 km, which implies that static strains will be much less than 100 ppb [*Wyatt*, 1988]; at these levels, the observed PDS from the 2009 Canal de Ballenas earthquake is at least 3–4 times but possibly 10–100 times larger than the static signal from the VLFE. For this reason, we first detrended the records based on the data seen between the origin time and the first surface-wave arrivals; we then applied a causal, lowpass filter [*Agnew and Hodgkinson*, 2007] to the detrended records to preserve the time-independence of these signals, for comparison with the timing of the VLFEs. Static offsets are computed from these filtered, detrended strain records (g), and are then transformed to tensor strain values (E) using the coupling equation:

$$E = Cg \tag{1}$$

As described above g is a matrix of strain timeseries from the instrument's 4 strain gauges:

$$g = [g_1, g_2, g_3, g_4]' \tag{2}$$

The matrix C is a 3×4 matrix of calibration coefficients determined by tidal analyses [e.g., *Hodgkinson et al.*, 2013]; it transforms g into tensor strain components, with coefficients that vary by station. The resulting matrix E contains the areal strain and two engineering shear strains in an east-north (e-n) coordinate reference system, where extensional strains are positive:

$$E = [E_{ee} + E_{nn}, E_{ee} - E_{nn}, 2E_{en}]' \tag{3}$$

For instance, the value E_{ee} represents uniaxial, extension in the east direction. Thus, the rms extension is found through the quadrature sum of the components of $0.5E$, or $E_{RMS} = \sqrt{(E_{ee}^2 + E_{nn}^2 + E_{en}^2)/3}$, and similarly the shear components of $0.5E$ give the maximum shear strain: $\tau_{max} = \sqrt{(E_{ee} - E_{nn})^2/4 + E_{en}^2}$. The calibration matrices (C) used for these strainmeters are from *Roeloffs* [2010] and *Hodgkinson et al.* [2013] as detailed in Table S3.

3 Results

In Cascadia, we detect three new seismic sources that are likely VLFEs (Figure 2). These sources generated coherent, transcontinental wavefields, and were detected by our surface wave detector [*de Groot-Hedlin and Hedlin*, 2015; *Fan et al.*, 2018]. With the measured centroid times and surface-wave propagation directions, we identify three seismic sources offshore Cascadia, E1–E3 (Figure 2). The VLFEs coincide with surface wave arrivals of the 3 August 2009 Mw 6.9 Canal de Ballenas earthquake.

The best resolved event (E3) occurred at 18:13:10 UTC, ~764 seconds after the Canal de Ballenas earthquake origin time; its epicenter is near the entrance of the Strait of Juan de Fuca, ~2360 km away from earthquake epicenter (Figure 1). Therefore, E3 occurred coinciding with the earthquake Rayleigh waves, assuming a group velocity of 3–3.5 km/s. Its coherent waveforms can be clearly identified from the aligned traces (Figure 3). All of the VLFE events (E1–E3) occurred immediately after the passing seismic waves from the Canal de Ballenas earthquake, and were most likely dynamically triggered by the earthquake. We could not analyze seismic data from stations in the near-field confidently because of the near-instantaneous triggering responses: the long lasting coda waves of the Canal de Ballenas earthquake masked signals of E1–E3 at stations in the Pacific Northwest (Figures 3,S1). However, none of the events (E1–E3) produced visible, high-frequency body-wave phases (Figure S1), nor are they listed in standard catalogs, refuting the possibility that instead they are regular earthquakes. Such a lack of high-frequency seismic radiation suggest that these sources are likely VLFEs.

We verify this hypothesis by modeling the E3 focal mechanism (Figure 4). The waveforms associated with E3 are well-separated from the surface waves of the Canal de Ballenas earthquake in the far-field, permitting such an analysis; the other two VLFEs are too difficult to model due to the poor signal-to-noise ratios of the records (Figures 3, S2). Therefore, we focus our discussions on event E3 in this study and only report the detections of E1 and E2 (Figure 2). The preferred solution suggests that E3 lasted less than 20 s (a point source) and has a mechanism with a strike of 125°, dip of 1°, and rake of -117° at a depth of 15 km (Figure 5). The subhorizontal dip of E3 deviates away from the local slab geometry and likely suffers uncertainties.

The focal mechanism and depth solution suffers from uncertainties because it is based on a catalog, and the teleseismic surface waves used for the analysis were filtered in a narrow period-band (Figure 4). Since the likely depth range for E3 is 15–25 km (Figures 6 and 8), it is difficult to determine how the source depth deviates from the plate interface geometry [*Hayes et al.*, 2018]. However, it is worth noting that the E3 depth range is shallower than the tremor and slow slip zone depths of 30–50 km [*Bartlow et al.*, 2011; *Bartlow*, 2020]. After resolving the focal mechanism and the event depth, we use the amplitude ratios between the synthetic waveforms and the observations to estimate the VLFE moment magnitude. The E3 event has an estimated moment magnitude (Mw) of 5.7 (0.5×10^{18} N $\cdot$ m, Figure 4), which is much larger than those of other VLFEs (M2.1–4.1) in the region [*Hutchison and Ghosh*, 2016; *Ide*, 2016].

At multiple stations near E3, we observe static strain offsets after the E3 occurrence (Figure 6). A table of observed offsets can be found in the Supplement. We ruled out the possibility that these are spurious strains [e.g., *Barbour et al.*, 2015] by confirming the absence of static offsets at distant stations in the region with similar dynamic strain amplitudes (Figure 9). We also note that the observed static strains are not apparent until soon after the seismically-determined origin time of E3 (Figure 6). With the source parameters, we model the static strains due to E3 with an edge dislocation in an elastic halfspace [*Okada*, 1985], and compare the model-predictions with observations at nearby strainmeter stations of the NOTA network (Figures 6 and 7). With the exception of station B003, the overall spatial pattern of the observed static strains from the other nine stations is consistent with the synthetic strains. This confirms the event E3 and its source model, suggesting that these strain data

represent the first set of direct observations of static crustal deformation associated with a VLFE at any subduction zone.

4 Discussion

4.1 Resolutions and Uncertainties

The detected VLFEs in Cascadia are unlikely to be data artifacts: their radiated surface waves, particularly from E3, span most of the United States (Figure 2) and the direct geodetic observations conclusively confirm E3 and that the event occurred near the seismically determined location (Figures 6 and 8). Further, E3 can be directly identified from aligned waveforms, furthering confirming its location (Figure 3).

In addition to triggered seismic events, heterogeneous subsurface structure can cause a secondary coherence surface wavefield by reflecting or converting the incoming waves [*Obara and Matsumura*, 2010; *Maeda et al.*, 2014; *Buehler et al.*, 2018; *Yu et al.*, 2017, 2021]. Here we considered the possibility that the detected VLFEs are actually scattered energy from the Canal de Ballenas event seismic waves rather than a unique local source. For example, the observations could have been from S-wave to surface-wave conversions that have been observed from the US west coast [*Buehler et al.*, 2018; *Yu et al.*, 2021]. However, we found that this hypothesis violates the observations in a number of ways. First, if the VLFEs are S-to-Rayleigh wave or P-to-Rayleigh wave scatterers, these seismic sources would occur upon the body wave arrivals. However, the observations show that the detected seismic sources occurred after the surface waves (Figure 3). Second, previous surface-wave reflections from a single scatter would last longer than 200 s [*Obara and Matsumura*, 2010], which contradicts to what we observe for the surface waves of E3 in Figure 3 (duration of E3 is less than 20 s). Lastly, if the detected triggered sources are structural heterogeneities (scatterers), they would cause the same scattering for earthquakes from the same region. In that case, the seismic sources detected by ALEUMA would be located at the same location and the measured propagation directions would be identical after large triggering earthquakes from the nearby region [*Obara and Matsumura*, 2010]. However, this is inconsistent with our observations (Figure S3). We observe no triggered seismic sources in Cascadia after the 2010 Mw 7.2 El Mayor-Cucapah earthquake, 2012 Mw 7.0 Baja California earthquake, or the 2019 Mw 7.0 Ridgecrest earthquake (Figure S3). These observations falsify the scattering hypothesis and confirm the observed VLFEs, particularly E3.

Overall there is good spatial agreement between the observed static strains and modeled strains (Figure 7a), and there is no apparent influence from peak dynamic strain levels (Figure 7b). However, observations from the closest station, B003, are notably smaller than suggested by the dislocation model. We believe this misfit arises for a few important reasons, namely the effects of ocean loading on the earth tides, and errors in source mechanism parameters. The loading of the crust by the ocean causes highly nonlinear distortions in the phases and amplitudes of tidal constituents near the land-sea interface [e.g., *Lambert*, 1970; *Farrell et al.*, 1973]. With strainmeter data located near the coast, it is notoriously difficult to model tidal strains needed for an accurate calibration procedure [see *Hodgkinson et al.*, 2013; *Kamigaichi et al.*, 2021]. Consequently, there are significant uncertainties in the strainmeter calibration coefficients in this region owing to their proximity to the coast. At present, the tidal models for all the stations considered here are adequate, with the exception of B003 [see *Roeloffs*, 2010; *Hodgkinson et al.*, 2013; *Reuveni et al.*, 2014]. The second major influence in near-source results comes from variations in focal mechanism parameters; these have a similarly strong influence on the spatial pattern of coseismic strain in the near-to-intermediate field, layered structure notwithstanding. For instance, the locations of nodes of null deformation are strongly influenced by strike and dip, and some stations are located close to these nodes, between lobes of significant deformation (e.g., Figure 6a) where small changes in strike or dip would have the strongest effect. Unfortunately, there are too few strainmeters near E3 to perform an independent source inversion; but, the current set of static strain obser-

vations can conclusively confirm the E3 occurrence and its relatively large moment magnitude.

Instead, to independently test the seismic-based location of E3, we forward modeled the same focal mechanism at every point on the Slab2.0 subduction zone interface [*Hayes et al.*, 2018] and calculated the source likelihood from the strain data misfit. Owing to station coverage there is a relatively broad zone of plausible source locations (Figure 7c). The uncertainty in the geodetic location is unavoidably large because additional stations are needed to rigorously constrain the source based on the static deformation pattern. There are two separate areas with a reduced Chi-squared (χ^2) misfit equal to 1, meaning that a source like E3 located in either region would fit the data equally well. One area sits within the seismic-derived uncertainty whereas the other falls far outside of it (Figure 7c). The seismic location uncertainty is estimated based on a very conservative criteria (within 25% of the misfit minimum instead of the commonly used 5% threshold), which likely overestimates the uncertainty ellipse; thus, the most likely location based on strain observations alone is within tens of kilometer of the seismic location (Figures 7c and 8). Further, teleseismic surface waves are sensitive to source depth, and a change of E3 depth from 15–20 km to 30–50 km or greater is also highly unlikely (Figure 4b).

We also compared the timing of the surface waves and VLFE detections with long-term strain records in Cascadia and the detected tremor events from the World Tremor Database (WTD)[*Idehara et al.*, 2014] in Figure 9. These data cannot definitively rule out deformation signals related to slow slip occurring prior to 2009/8/3, but they do show that if slow slip related to the 2009 ETS event initiated before these arrivals, the strain signals are undetectable relative to the non-tectonic noise seen at these stations. Further, the tremor rate increases roughly 10 hours after the triggered VLFE events, as the slow slip event is apparently developing; this is juxtaposed by a multi-day quiescence and a lack of slip-related signals in GNSS data prior to the passing seismic waves (Figure 9c).

4.2 Triggering and Interaction

Slow earthquakes interact and trigger each other frequently [*Obara and Kato*, 2016]. For example, slow slip events can drive tremor, causing ETS events in Cascadia [*Rogers and Dragert*, 2003; *Bartlow et al.*, 2011], and VLFEs have been triggered by long-term SSEs offshore Japan [*Hirose et al.*, 2010; *Araki et al.*, 2017; *Katakami et al.*, 2020]. The close spatiotemporal correlation between the observed VLFEs and the 2009 slow slip event in Cascadia suggests that they are likely physically related [*Rubinstein et al.*, 2009]. One possibility is that these large-magnitude VLFEs, caused by the passing seismic waves, may have initiated a slow slip event which eventually developed into the 2009 Cascadia ETS event. Presently, we cannot confirm this cascading process, as neither GNSS stations or borehole strainmeters in Cascadia detected slip-related deformation before the 2009 ETS event above background noise levels (Figure 9). Such ambiguity cannot exclude that there were slow slips triggered by the passing seismic wave, which would suggest that the 2009 ETS event was triggered by the Canal de Ballenas earthquake. A long-term, systematic investigation of the onset timing of Cascadia ETS is necessary to illuminate the susceptibility of slow slip events in the region due to remote earthquakes. Despite the ambiguity in the timing of the 2009 ETS event relative to the VLFEs, our observations suggest that complex slip interactions may occur more frequently at Cascadia than previously documented.

Slow earthquakes can be susceptible to triggering due to small external stress perturbations [*Obara and Kato*, 2016; *Katakami et al.*, 2020; *Araki et al.*, 2017], which is best illustrated by the sensitivity of tremor occurrence to Earth tides and passing seismic waves [*Rubinstein et al.*, 2008, 2009; *Hawthorne and Rubin*, 2010; *Chao et al.*, 2013; *Houston*, 2015; *Miyazawa*, 2019]. For example, remote triggering of VLFEs by surface waves from a moderate to large, distant earthquake has been reported in the Nankai subduction zone [*Miyazawa*, 2019]. Passing seismic waves also triggered aseismic slip events on the San Andreas fault

that led to migrating tremor [*Shelly et al.*, 2011]. Such dynamically triggered cascading slip events may be similar to what we observe in this study. With direct measurements of dynamic strain, we estimate the dynamic stresses associated with the passing seismic waves. Assuming a shear modulus of 30 GPa, the dynamic, elastic stress perturbations from the Canal de Ballenas earthquake were likely ~20–30 kPa at E3. The true triggering stresses at E3 could vary within a few percent depending on the depth dependence of surface waves, fault geometry, fault frictional properties and pre-stress, and dynamic pore pressure effects. Other earthquakes with similar magnitudes near the Canal de Ballenas earthquake did not trigger events in Cascadia (Figure S3), suggesting that earthquake rupture process might play an important role in generating strong teleseismic ground motions that can cause dynamic triggering cases.

The observed triggering process suggests that the E3 patch in the fault gap was at a critical state prior to the surface wave arrivals. Alternatively, the fault could have been very weak, such that the dynamic stress changes from the Canal de Ballenas earthquake were sufficient to trigger an unstable dynamic rupture; in that case, triggered VLFEs would be a commonly-observed phenomenon rather than the rarely reported phenomenon they are presently [*Miyazawa*, 2019]. Nonetheless, in this study, the observed VLFEs show that in between the seismogenic zone and the ETS zone, some patches of the megathrust fault gap are capable of hosting M5.7 seismic events that are sensitive to transient stress perturbations.

4.3 Physical Conditions in Between the Seismogenic and Tremor Zones

Event E3 occurred at depths shallower than other slow earthquakes in the Cascadia subduction zone [*Gomberg et al.*, 2010; *Brudzinski and Allen*, 2007]. Interestingly, neither tremor nor slow slip signals were detected in the region during these triggered VLFEs [*Wech and Creager*, 2008; *Bartlow et al.*, 2011]; this behavior differs from typical VLFEs in this region that are often coincident with tremor and slow slip [e.g., *Hutchison and Ghosh*, 2016; *Ide*, 2016]. The relatively shallow depth of E3 corresponds to the deepest part of the locked zone – a gap in between the seismogenic zone and the tremor zone [*Hyndman and Wang*, 1995; *Wang et al.*, 2003; *Priest et al.*, 2010; *Schmalzle et al.*, 2014; *Bruhat and Segall*, 2016]. In northern Cascadia, slow slip events have penetrated upward into this gap zone during previous ETS events, but tremor has been scarce there [*Wang et al.*, 2008; *Wech et al.*, 2009; *Hall et al.*, 2018]. Further, sporadic weak slips are observed in this gap zone across all of Cascadia [*Bartlow*, 2020; *Nuyen and Schmidt*, 2021].

Given the magnitude and location of E3, our observed VLFEs may relate to these aseismic slips, and in combination, their slip contributions may be analogous to the longer-term SSEs in Nankai, where tremors do not overlap with SSEs in such a gap zone [*Hirose et al.*, 2010; *Kobayashi*, 2014]. However, the occurrence of E3 also suggests that this gap region is not creeping steadily or slipping aseismically [*Holtkamp and Brudzinski*, 2010; *Hyndman*, 2013; *Schmalzle et al.*, 2014]. Instead, the gap zone is likely partially locked and rupture might be able to propagate sufficiently fast at some patches. Such a locking transition zone is physically intuitive, but the type of seismic slip events needed to confirm its properties are rarely observed in the region. The magnitude of E3 indicates that the fault's strength may increase in the gap zone, compared to the ETS zone, suggesting that loading stresses from the slow slip events fail to generate seismic failures during conventional Cascadia ETS events, possibly due to the size of the locked fault patch and frictional properties [*Hall et al.*, 2018].

Conceptually, the gap zone may represent a semi-frictional phase connecting the seismogenic and the tremor zone [*Gao and Wang*, 2017], which may be comprised of large strong fault patches that can generate VLFEs, but with a lower level of asperity heterogeneity on fault than the tremor zone [e.g., *Wu et al.*, 2019], surrounded by a ductile matrix [*Chestler and Creager*, 2017] that could slip aseismically [*Wang et al.*, 2008; *Hall et al.*, 2018]. Therefore, our observed VLFEs could be a manifestation of a transitioning semi-frictional be-

haviour as an intermediate stage between seismic rupture and viscous creep [*Gao and Wang*, 2017]. Such cases may explain our observed VLFEs with a lack of tremor activity in the gap zone, presumably related to the nonstationary shear stress rates inferred from decadally-averaged crustal deformation rates [*Bruhat and Segall*, 2016].

From the seismogenic zone to the tremor zone in northern Cascadia, there is a change in the reflection character on seismic images from a thin sharp reflection band to a broad reflection band [*Nedimović et al.*, 2003]. The seismic images were obtained from active surveys that were ~50 km north of E3, and the images show prominent broad reflectors at a depth range of 15–25 km, coinciding with the gap zone [*Nedimović et al.*, 2003]. Such reflectors are regionally extensive and may represent interlayered mafic and/or sedimentary rocks or intensely sheared sediments with trapped fluids [*Yorath et al.*, 1985; *Clowes et al.*, 1987; *Calvert and Clowes*, 1990], and E3 seems to relate to these reflectors. Shearing and fluid can lead to prevalent ductile banding there, which would produce a thick semi-frictional and semi-ductile zone where either frictional or ductile slip can occur depending on the local conditions [*Nedimović et al.*, 2003; *Gao and Wang*, 2017]. In such a scenario, some kilometer-scale sub-horizontal fault patches that are confined with high fluid pressure would preferably slip seismically, which might have been the structural cause of the observed VLFEs.

Seismic sources in the region such as E3 might be used to infer dimensions and stress states of the locked fault patches. In conjunction with the sporadic weak slip in the zone [*Bartlow*, 2020; *Nuyen and Schmidt*, 2021], the few VLFEs (E1–E3) seem to suggest that fault properties of the gap zone are highly heterogeneous. In that case certain patches could slip fast, possibly allowing a deep rupture extent at these spots, which could change the distribution of strong shaking and cause more intense ground motion along the densely populated margin [*Melgar et al.*, 2016; *Frankel et al.*, 2018; *Wirth et al.*, 2018; *Ramos and Huang*, 2019]. However, given the relatively large location uncertainties for these VLFEs, future systematic investigations are warranted to delineate the downdip rupture limit of large megathrust earthquakes in Cascadia.

4.4 Breakdown of the Slow Earthquake Scaling Relationship

It has been suggested that slow earthquakes, including VLFEs, follow an apparent moment-duration scaling relationship where the moment rate of these events is likely constant and the final seismic moment is proportional to the characteristic duration [*Ide et al.*, 2007]. This would be different from the scaling of regular earthquakes, for which moment scales linearly with the cube of the characteristic duration [*Abercrombie*, 1995; *Houston*, 2001]. The difference was hypothesized to arise from different rupture dynamics between slow and regular earthquakes [*Ide et al.*, 2007]. Further, slow earthquakes are thought to rupture faster than the plate movement rate, but their rupture speeds cannot accelerate to those of typical earthquakes [*Gao et al.*, 2012; *Bletery et al.*, 2017]. If those empirical scaling relationships hold true, we would expect a M5.7 VLFE or slow earthquake to last from 6 days to a month [*Ide et al.*, 2007]. Consequentially, the rupture speed of such an event would be too slow to generate seismic signals that can be observed in the far field [*Gao et al.*, 2012].

Here, seismic and geodetic observations directly refute such slow earthquake scaling relationships: waveform modeling shows that E3 was likely a transient event, whose duration is much less than the predicted duration from the slow earthquake scaling relationship (Figure 4) but is in closer agreement with the scaling of regular earthquakes [*Houston*, 2001], and static strains developed within the duration timescale (Figure 6). Our observations agree well with recent findings showing that slow slip events and regular earthquakes follow similar scaling laws that the slow slip moment scales with the slip duration cubed [*Michel et al.*, 2019; *Frank and Brodsky*, 2019]. Numerical simulations also show that slow self-arresting rupture within the rupture patch would generate VLFEs with source properties following the cubed duration scaling [*Wei et al.*, 2021]. Collectively, these results show that slow and regu-

lar earthquakes are likely governed by similar dynamic properties [*Michel et al.*, 2019; *Frank and Brodsky*, 2019]. Alternatively, if the events detected here are not actually VLFEs, event E3 is still not a typical earthquake as no high-frequency seismic radiation was observed at seismic stations in the Pacific Northwest (Figures S1 and S4). Our reported VLFEs seem to be distinct from other Cascadia VLFEs or slow earthquakes in Nankai [*Ghosh et al.*, 2015; *Hutchison and Ghosh*, 2016; *Obara and Kato*, 2016; *Ide et al.*, 2007]: they do not seem to be accompanied by tremor or SSEs but are independent slip events ~10–15 km shallower than typical VLFEs in the region. Further, E3 is the largest magnitude that has been reported at all subduction zones, producing measurable static geodetic signals. Our findings raise new questions about the physical nature of the gap zone: is there a new class of slip events that represents a bridge between future megathrust earthquakes and tremor in Cascadia?

5 Conclusions

By analyzing continuous data from seismic stations across the United States, we identify and locate 3 previously unknown VLFEs that are close to the 2009 Cascadia slow slip event and that occurred roughly three days before the initiation of the associated tremor activity. One VLFE is located in the critical gap zone with a moment magnitude of 5.7, which is the largest VLFE that has been identified across all subduction zones. Further, this is the first time that a VLFE is recorded geodetically, with an array of strainmeters showing clear deformation signals associated with the event. Our findings suggest that some patches of the gap zone are capable of hosting large, fast slip events, indicating possible deep ruptures at sporadic spots in Cascadia. Our observed VLFEs also show that the Cascadia megathrust is weak and is sensitive to transient stress perturbations. Lastly, the identified VLFEs challenge the current understanding of slow earthquake physics, with characteristics that deviate away from the empirical scaling relations of slow earthquakes.

Open Research

The seismic data were provided by Data Management Center (DMC) of the Incorporated Research Institutions for Seismology (IRIS). The facilities of IRIS Data Services, and specifically the IRIS Data Management Center, were used for access to waveforms, related metadata, and/or derived products used in this study. IRIS Data Services are funded through the Seismological Facilities for the Advancement of Geoscience and EarthScope (SAGE) Proposal of the National Science Foundation (NSF) under Cooperative Agreement EAR-1261681. High-frequency strain data from the Network of the Americas (NOTA) network were also obtained from the IRIS DMC; this material is based on services provided by the Geodesy Advancing Geosciences and EarthScope (GAGE) facility, operated by UNAVCO, Inc., with support from the NSF and the National Aeronautics and Space Administration (NASA) under NSF Cooperative Agreement EAR-1724794. NOTA Level 2 strain and GNSS data were obtained from UNAVCO web-services (`https://www.unavco.org/data/web-services/web-services.html`). The tremor catalog is obtained from the Pacific Northwest Seismic Network and the World Tremor Database (`http://www-solid.eps.s.u-tokyo.ac.jp/~idehara/wtd0/Welcome.html`). The earthquake catalogs used in this study are from the Global Centroid Moment Tensor project (GCMT) [*Ekström et al.*, 2012].

Acknowledgments

We thank David Shelly, Joan Gomberg, Kelin Wang, the three anonymous reviewers, and the editor Thorsten Becker for thoughtful, constructive comments that led to significant improvements to this manuscript. W.F. was supported by NSF EAR-2143413. Any use of trade, firm, or product names is for descriptive purposes only and does not imply endorsement by the U.S. government.

References

Abercrombie, R. E. (1995), Earthquake source scaling relationships from −1 to 5 ML using seismograms recorded at 2.5 km depth, *Journal of Geophysical Research: Solid Earth*, *100*(B12), 24,015–24,036.

Agnew, D. C., and K. Hodgkinson (2007), Designing compact causal digital filters for low-frequency strainmeter data, *Bulletin of the Seismological Society of America*, *97*(1B), 91–99, doi:10.1785/0120060088.

Agnew, D. C., and F. K. Wyatt (2014), Dynamic strains at regional and teleseismic distances, *Bulletin of the Seismological Society of America*, *104*(4), 1846–1859, doi:10.1785/0120140007.

Araki, E., D. M. Saffer, A. J. Kopf, L. M. Wallace, T. Kimura, Y. Machida, S. Ide, E. Davis, and (2017), Recurring and triggered slow-slip events near the trench at the Nankai Trough subduction megathrust, *Science*, *356*(6343), 1157–1160, doi:10.1126/science.aan3120.

Barbour, A. J., and B. W. Crowell (2017), Dynamic strains for earthquake source characterization, *Seismological Research Letters*, *88*(2A), 354–370.

Barbour, A. J., D. C. Agnew, and F. K. Wyatt (2015), Coseismic strains on Plate Boundary Observatory borehole strainmeters in Southern California, *Bulletin of the Seismological Society of America*, *105*(1), 431–444, doi:10.1785/0120140199.

Bartlow, N. M. (2020), A long-term view of Episodic Tremor and Slip in Cascadia, *Geophysical Research Letters*, *47*(3), e2019GL085,303, doi:10.1029/2019GL085303.

Bartlow, N. M., S. Miyazaki, A. M. Bradley, and P. Segall (2011), Space-time correlation of slip and tremor during the 2009 Cascadia slow slip event, *Geophysical Research Letters*, *38*(18).

Bletery, Q., A. M. Thomas, J. C. Hawthorne, R. M. Skarbek, A. W. Rempel, and R. D. Krogstad (2017), Characteristics of secondary slip fronts associated with slow earthquakes in Cascadia, *Earth and Planetary Science Letters*, *463*, 212–220.

Bostock, M., A. Royer, E. Hearn, and S. Peacock (2012), Low frequency earthquakes below southern Vancouver Island, *Geochemistry, Geophysics, Geosystems*, *13*(11).

Brown, J. R., G. C. Beroza, S. Ide, K. Ohta, D. R. Shelly, S. Y. Schwartz, W. Rabbel, M. Thorwart, and H. Kao (2009), Deep low-frequency earthquakes in tremor localize to the plate interface in multiple subduction zones, *Geophysical Research Letters*, *36*(19).

Brudzinski, M. R., and R. M. Allen (2007), Segmentation in episodic tremor and slip all along Cascadia, *Geology*, *35*(10), 907–910.

Bruhat, L., and P. Segall (2016), Coupling on the northern Cascadia subduction zone from geodetic measurements and physics-based models, *Journal of Geophysical Research: Solid Earth*, *121*(11), 8297–8314.

Buehler, J., N. Mancinelli, and P. Shearer (2018), S-to-Rayleigh wave scattering from the continental margin observed at USArray, *Geophysical Research Letters*, *45*(10), 4719–4724.

Calvert, A., and R. Clowes (1990), Deep, high-amplitude reflections from a major shear zone above the subducting Juan de Fuca plate, *Geology*, *18*(11), 1091–1094.

Castro, R. R., C. Valdés-González, P. Shearer, V. Wong, L. Astiz, F. Vernon, A. Pérez-Vertti, and A. Mendoza (2011), The 3 August 2009 Mw 6.9 Canal de Ballenas region, Gulf of California, earthquake and its aftershocks, *Bulletin of the Seismological Society of America*, *101*(3), 929–939.

Chao, K., Z. Peng, H. Gonzalez-Huizar, C. Aiken, B. Enescu, H. Kao, A. A. Velasco, K. Obara, and T. Matsuzawa (2013), A Global search for triggered tremor following the 2011 Mw 9.0 Tohoku earthquake, *Bulletin of the Seismological Society of America*, *103*(2 B), 1551–1571, doi:10.1785/0120120171.

Chestler, S., and K. Creager (2017), A model for low-frequency earthquake slip, *Geochemistry, Geophysics, Geosystems*, *18*(12), 4690–4708.

Clowes, R., M. Brandon, A. Green, C. Yorath, A. S. Brown, E. Kanasewich, and C. Spencer (1987), LITHOPROBE–southern Vancouver Island: Cenozoic subduction complex im-

aged by deep seismic reflections, *Canadian Journal of Earth Sciences*, *24*(1), 31–51.

de Groot-Hedlin, C. D., and M. A. Hedlin (2015), A method for detecting and locating geophysical events using groups of arrays, *Geophysical Journal International*, *203*(2), 960–971.

Dragert, H., and K. Wang (2011), Temporal evolution of an episodic tremor and slip event along the northern Cascadia margin, *Journal of Geophysical Research: Solid Earth*, *116*(B12).

Dragert, H., K. Wang, and T. S. James (2001), A silent slip event on the deeper Cascadia subduction interface, *Science*, *292*(5521), 1525–1528.

Driel, M. v., L. Krischer, S. C. Stähler, K. Hosseini, and T. Nissen-Meyer (2015), Instaseis: Instant global seismograms based on a broadband waveform database, *Solid Earth*, (2), 701–717.

Dziewonski, A. M., and D. L. Anderson (1981), Preliminary reference Earth model, *Physics of the earth and planetary interiors*, *25*(4), 297–356.

Ekström, G., M. Nettles, and A. Dziewoński (2012), The global CMT project 2004–2010: Centroid-moment tensors for 13,017 earthquakes, *Physics of the Earth and Planetary Interiors*, *200*, 1–9.

Fan, W., C. D. de Groot-Hedlin, M. A. Hedlin, and Z. Ma (2018), Using surface waves recorded by a large mesh of three-element arrays to detect and locate disparate seismic sources, *Geophysical Journal International*, *215*(2), 942–958.

Fan, W., J. J. McGuire, C. D. de Groot-Hedlin, M. A. Hedlin, S. Coats, and J. W. Fiedler (2019), Stormquakes, *Geophysical Research Letters*, *46*(22), 12,909–12,918.

Fan, W., J. J. McGuire, and P. M. Shearer (2020), Abundant spontaneous and dynamically triggered submarine landslides in the Gulf of Mexico, *Geophysical Research Letters*, *47*(12), e2020GL087,213.

Farrell, W. E., A. H. Cook, R. V. Jones, and G. C. P. King (1973), A Discussion on the measurement and interpretation of changes of strain in the Earth - Earth tides, ocean tides and tidal loading, *Philosophical Transactions of the Royal Society of London. Series A, Mathematical and Physical Sciences*, *274*(1239), 253–259, doi:10.1098/rsta.1973.0050.

Frank, W. B., and E. E. Brodsky (2019), Daily measurement of slow slip from low-frequency earthquakes is consistent with ordinary earthquake scaling, *Science advances*, *5*(10), eaaw9386.

Frankel, A., E. Wirth, N. Marafi, J. Vidale, and W. Stephenson (2018), Broadband synthetic seismograms for magnitude 9 earthquakes on the Cascadia megathrust based on 3D simulations and stochastic synthetics, Part 1: Methodology and overall results, *Bulletin of the Seismological Society of America*, *108*(5A), 2347–2369.

Gao, H., D. A. Schmidt, and R. J. Weldon (2012), Scaling relationships of source parameters for slow slip events, *Bulletin of the Seismological Society of America*, *102*(1), 352–360.

Gao, X., and K. Wang (2017), Rheological separation of the megathrust seismogenic zone and episodic tremor and slip, *Nature*, *543*(7645), 416–419.

Ghosh, A., E. Huesca-Pérez, E. Brodsky, and Y. Ito (2015), Very low frequency earthquakes in Cascadia migrate with tremor, *Geophysical Research Letters*, *42*(9), 3228–3232.

Gladwin, M. T. (1984), High-precision multicomponent borehole deformation monitoring, *Review of Scientific Instruments*, *55*(12), 2011–2016, doi:10.1063/1.1137704.

Gomberg, J., C. 2007, and B. W. Group (2010), Slow-slip phenomena in Cascadia from 2007 and beyond: A review, *GSA Bulletin*, *122*(7-8), 963–978.

Hall, K., H. Houston, and D. Schmidt (2018), Spatial comparisons of tremor and slow slip as a constraint on fault strength in the northern Cascadia subduction zone, *Geochemistry, Geophysics, Geosystems*, *19*(8), 2706–2718.

Hawthorne, J. C., and A. M. Rubin (2010), Tidal modulation of slow slip in Cascadia, *Journal of Geophysical Research: Solid Earth*, *115*(B9).

Hayes, G. P., G. L. Moore, D. E. Portner, M. Hearne, H. Flamme, M. Furtney, and G. M. Smoczyk (2018), Slab2, a comprehensive subduction zone geometry model, *Science*, *362*(6410), 58–61.

Hill, D. P. (2008), Dynamic stresses, Coulomb failure, and remote triggering, *Bulletin of the Seismological Society of America*, *98*(1), 66–92.

Hirose, H., Y. Asano, K. Obara, T. Kimura, T. Matsuzawa, S. Tanaka, and T. Maeda (2010), Slow earthquakes linked along dip in the Nankai subduction zone, *Science*, *330*(6010), 1502–1502.

Hodgkinson, K., J. Langbein, B. Henderson, D. Mencin, and A. Borsa (2013), Tidal calibration of plate boundary observatory borehole strainmeters, *Journal of Geophysical Research: Solid Earth*, *118*(1), 447–458, doi:10.1029/2012jb009651.

Holtkamp, S., and M. R. Brudzinski (2010), Determination of slow slip episodes and strain accumulation along the Cascadia margin, *Journal of Geophysical Research: Solid Earth*, *115*(B4).

Houston, H. (2001), Influence of depth, focal mechanism, and tectonic setting on the shape and duration of earthquake source time functions, *Journal of Geophysical Research: Solid Earth*, *106*(B6), 11,137–11,150.

Houston, H. (2015), Low friction and fault weakening revealed by rising sensitivity of tremor to tidal stress, *Nature Geoscience*, *8*(5), 409–415.

Hutchison, A. A., and A. Ghosh (2016), Very low frequency earthquakes spatiotemporally asynchronous with strong tremor during the 2014 episodic tremor and slip event in Cascadia, *Geophysical Research Letters*, *43*(13), 6876–6882.

Hyndman, R., and K. Wang (1995), The rupture zone of Cascadia great earthquakes from current deformation and the thermal regime, *Journal of Geophysical Research: Solid Earth*, *100*(B11), 22,133–22,154.

Hyndman, R. D. (2013), Downdip landward limit of Cascadia great earthquake rupture, *Journal of Geophysical Research: Solid Earth*, *118*(10), 5530–5549.

Ide, S. (2016), Characteristics of slow earthquakes in the very low frequency band: Application to the Cascadia subduction zone, *Journal of Geophysical Research: Solid Earth*, *121*(8), 5942–5952.

Ide, S., G. C. Beroza, D. R. Shelly, and T. Uchide (2007), A scaling law for slow earthquakes, *Nature*, *447*(7140), 76–79.

Idehara, K., S. Yabe, and S. Ide (2014), Regional and global variations in the temporal clustering of tectonic tremor activity, *Earth, Planets and Space*, *66*(1), 1–10, doi:10.1186/1880-5981-66-66.

Ito, Y., and K. Obara (2006), Dynamic deformation of the accretionary prism excites very low frequency earthquakes, *Geophysical Research Letters*, *33*(2).

Ito, Y., K. Obara, K. Shiomi, S. Sekine, and H. Hirose (2007), Slow earthquakes coincident with episodic tremors and slow slip events, *Science*, *315*(5811), 503–506.

Kamigaichi, O., N. Matsumoto, and F. Hirose (2021), Green's function at depth of borehole observation required for precise estimation of the effect of ocean tidal loading near coasts, *Geophysical Journal International*, doi:10.1093/gji/ggab216, ggab216.

Kao, H., K. Wang, H. Dragert, J. Y. Kao, and G. Rogers (2010), Estimating seismic moment magnitude (Mw) of tremor bursts in northern Cascadia: Implications for the "seismic efficiency" of episodic tremor and slip, *Geophysical Research Letters*, *37*(19).

Katakami, S., Y. Kaneko, Y. Ito, and E. Araki (2020), Stress Sensitivity of Instantaneous Dynamic Triggering of Shallow Slow Slip Events, *Journal of Geophysical Research: Solid Earth*, *125*(6), e2019JB019,178, doi:https://doi.org/10.1029/2019JB019178, e2019JB019178 2019JB019178.

Kobayashi, A. (2014), A long-term slow slip event from 1996 to 1997 in the Kii Channel, Japan, *Earth, Planets and Space*, *66*(1), 1–7.

Lambert, A. (1970), The Response of the Earth to loading by the ocean tides around Nova Scotia, *Geophysical Journal International*, *19*(5), 449–477, doi:10.1111/j.1365-246X.1970.tb00152.x.

Maeda, T., T. Furumura, and K. Obara (2014), Scattering of teleseismic P-waves by the Japan Trench: A significant effect of reverberation in the seawater column, *Earth and Planetary Science Letters*, *397*, 101–110.

Melgar, D., R. J. LeVeque, D. S. Dreger, and R. M. Allen (2016), Kinematic rupture scenarios and synthetic displacement data: An example application to the Cascadia subduction zone, *Journal of Geophysical Research: Solid Earth*, *121*(9), 6658–6674.

Michel, S., A. Gualandi, and J.-P. Avouac (2019), Similar scaling laws for earthquakes and Cascadia slow-slip events, *Nature*, *574*(7779), 522–526.

Miyazawa, M. (2019), Bayesian approach for detecting dynamically triggered very low-frequency earthquakes in the Nankai subduction zone and application to the 2016 M w 5.9 off-Kii Peninsula earthquake, Japan, *Geophysical Journal International*, *217*(2), 1123–1140.

Nedimović, M. R., R. D. Hyndman, K. Ramachandran, and G. D. Spence (2003), Reflection signature of seismic and aseismic slip on the northern Cascadia subduction interface, *Nature*, *424*(6947), 416–420.

Nissen-Meyer, T., M. v. Driel, S. Stähler, K. Hosseini, S. Hempel, L. Auer, A. Colombi, and A. Fournier (2014), AxiSEM: broadband 3-D seismic wavefields in axisymmetric media, *Solid Earth*, (1), 425–445.

Nuyen, C. P., and D. A. Schmidt (2021), Filling the gap in Cascadia: The emergence of low-amplitude long-term slow slip, *Geochemistry, Geophysics, Geosystems*, *22*(3), e2020GC009,477.

Obara, K., and Y. Ito (2005), Very low frequency earthquakes excited by the 2004 off the Kii peninsula earthquakes: A dynamic deformation process in the large accretionary prism, *Earth, Planets and Space*, *57*(4), 321–326.

Obara, K., and A. Kato (2016), Connecting slow earthquakes to huge earthquakes, *Science*, *353*(6296), 253–257, doi:10.1126/science.aaf1512.

Obara, K., and M. Matsumura (2010), Reverse propagation of surface waves reflected from seamounts in the Northwestern Pacific, *Bulletin of the Seismological Society of America*, *100*(3), 1342–1349.

Okada, Y. (1985), Surface deformation due to shear and tensile faults in a half-space, *Bulletin of the seismological society of America*, *75*(4), 1135–1154.

Peng, Z., and J. Gomberg (2010), An integrated perspective of the continuum between earthquakes and slow-slip phenomena, *Nature geoscience*, *3*(9), 599–607.

Plattner, C., R. Malservisi, F. Amelung, T. H. Dixon, M. Hackl, A. Verdecchia, P. Lonsdale, F. Suarez-Vidal, and J. Gonzalez-Garcia (2015), Space geodetic observation of the deformation cycle across the Ballenas Transform, Gulf of California, *Journal of Geophysical Research: Solid Earth*, *120*(8), 5843–5862.

Porritt, R. W., R. M. Allen, D. C. Boyarko, and M. R. Brudzinski (2011), Investigation of Cascadia segmentation with ambient noise tomography, *Earth and Planetary Science Letters*, *309*(1), 67–76, doi:https://doi.org/10.1016/j.epsl.2011.06.026.

Priest, G. R., C. Goldfinger, K. Wang, R. C. Witter, Y. Zhang, and A. M. Baptista (2010), Confidence levels for tsunami-inundation limits in northern Oregon inferred from a 10,000-year history of great earthquakes at the Cascadia subduction zone, *Natural Hazards*, *54*(1), 27–73.

Ramos, M. D., and Y. Huang (2019), How the transition region along the Cascadia megathrust influences coseismic behavior: Insights from 2-D dynamic rupture simulations, *Geophysical Research Letters*, *46*(4), 1973–1983.

Reuveni, Y., S. Kedar, A. Moore, and F. Webb (2014), Analyzing slip events along the Cascadia margin using an improved subdaily GPS analysis strategy, *Geophysical Journal International*, *198*(3), 1269–1278, doi:10.1093/gji/ggu208.

Roeloffs, E. (2010), Tidal calibration of Plate Boundary Observatory borehole strainmeters: Roles of vertical and shear coupling, *Journal of Geophysical Research: Solid Earth*, *115*(B6), doi:10.1029/2009JB006407.

Rogers, G., and H. Dragert (2003), Episodic tremor and slip on the Cascadia subduction zone: The chatter of silent slip, *Science*, *300*(5627), 1942–1943.

Rubinstein, J. L., M. La Rocca, J. E. Vidale, K. C. Creager, and A. G. Wech (2008), Tidal modulation of nonvolcanic tremor, *Science*, *319*(5860), 186–189.

Rubinstein, J. L., J. Gomberg, J. E. Vidale, A. G. Wech, H. Kao, K. C. Creager, and G. Rogers (2009), Seismic wave triggering of nonvolcanic tremor, episodic tremor and slip, and earthquakes on Vancouver Island, *Journal of Geophysical Research: Solid Earth*, *114*(B2).

Schmalzle, G. M., R. McCaffrey, and K. C. Creager (2014), Central Cascadia subduction zone creep, *Geochemistry, Geophysics, Geosystems*, *15*(4), 1515–1532.

Shelly, D. R., Z. Peng, D. P. Hill, and C. Aiken (2011), Triggered creep as a possible mechanism for delayed dynamic triggering of tremor and earthquakes, *Nature Geoscience*, *4*(6), 384.

Sweet, J. R., K. C. Creager, H. Houston, and S. R. Chestler (2019), Variations in Cascadia low-frequency earthquake behavior with downdip distance, *Geochemistry, Geophysics, Geosystems*, *20*(2), 1202–1217.

U.S. Geological Survey (2017), Advanced National Seismic System (ANSS) Comprehensive Catalog of Earthquake Events and Products, doi:10.5066/F7MS3QZH, https://earthquake.usgs.gov/earthquakes/search/.

Walton, M. A., L. M. Staisch, T. Dura, J. K. Pearl, B. Sherrod, J. Gomberg, S. Engelhart, A. Tréhu, J. Watt, J. Perkins, et al. (2021), Toward an Integrative Geological and Geophysical View of Cascadia Subduction Zone Earthquakes, *Annual Review of Earth and Planetary Sciences*, *49*.

Wang, K., and A. M. Tréhu (2016), Invited review paper: Some outstanding issues in the study of great megathrust earthquakes–The Cascadia example, *Journal of Geodynamics*, *98*, 1–18.

Wang, K., R. Wells, S. Mazzotti, R. D. Hyndman, and T. Sagiya (2003), A revised dislocation model of interseismic deformation of the Cascadia subduction zone, *Journal of Geophysical Research: Solid Earth*, *108*(B1).

Wang, K., H. Dragert, H. Kao, and E. Roeloffs (2008), Characterizing an "uncharacteristic" ETS event in northern Cascadia, *Geophysical Research Letters*, *35*(15).

Wech, A. G., and N. M. Bartlow (2014), Slip rate and tremor genesis in Cascadia, *Geophysical Research Letters*, *41*(2), 392–398.

Wech, A. G., and K. C. Creager (2008), Automated detection and location of Cascadia tremor, *Geophysical Research Letters*, *35*(20).

Wech, A. G., K. C. Creager, and T. I. Melbourne (2009), Seismic and geodetic constraints on Cascadia slow slip, *Journal of Geophysical Research: Solid Earth*, *114*(B10).

Wei, X., J. Xu, Y. Liu, and X. Chen (2021), The slow self-arresting nature of low-frequency earthquakes, *Nature communications*, *12*(1), 1–9.

Wirth, E. A., A. D. Frankel, N. Marafi, J. E. Vidale, and W. J. Stephenson (2018), Broadband synthetic seismograms for magnitude 9 earthquakes on the Cascadia megathrust based on 3D simulations and stochastic synthetics, Part 2: Rupture parameters and variability, *Bulletin of the Seismological Society of America*, *108*(5A), 2370–2388.

Wu, B., D. D. Oglesby, A. Ghosh, and B. Li (2019), A dynamic rupture source model for very low-frequency earthquake signal without detectable nonvolcanic tremors, *Geophysical Research Letters*, *46*(21), 11,934–11,943.

Wyatt, F. K. (1988), Measurements of coseismic deformation in Southern California: 1972-1982, *J. Geophys. Res.*, *93*(B7), 7923–7942, doi:10.1029/JB093iB07p07923.

Yorath, C., A. Green, R. Clowes, A. S. Brown, M. Brandon, E. Kanasewich, R. Hyndman, and C. Spencer (1985), Lithoprobe, southern Vancouver Island: Seismic reflection sees through Wrangellia to the Juan de Fuca plate, *Geology*, *13*(11), 759–762.

Yu, C., Z. Zhan, E. Hauksson, and E. S. Cochran (2017), Strong SH-to-love wave scattering off the Southern California continental borderland, *Geophysical Research Letters*, *44*(20), 10–208.

Yu, C., J. C. Castellanos, and Z. Zhan (2021), Imaging strong lateral heterogeneities across the contiguous US using body-to-surface wave scattering, *Journal of Geophysical Research. Solid Earth*, *126*(1).

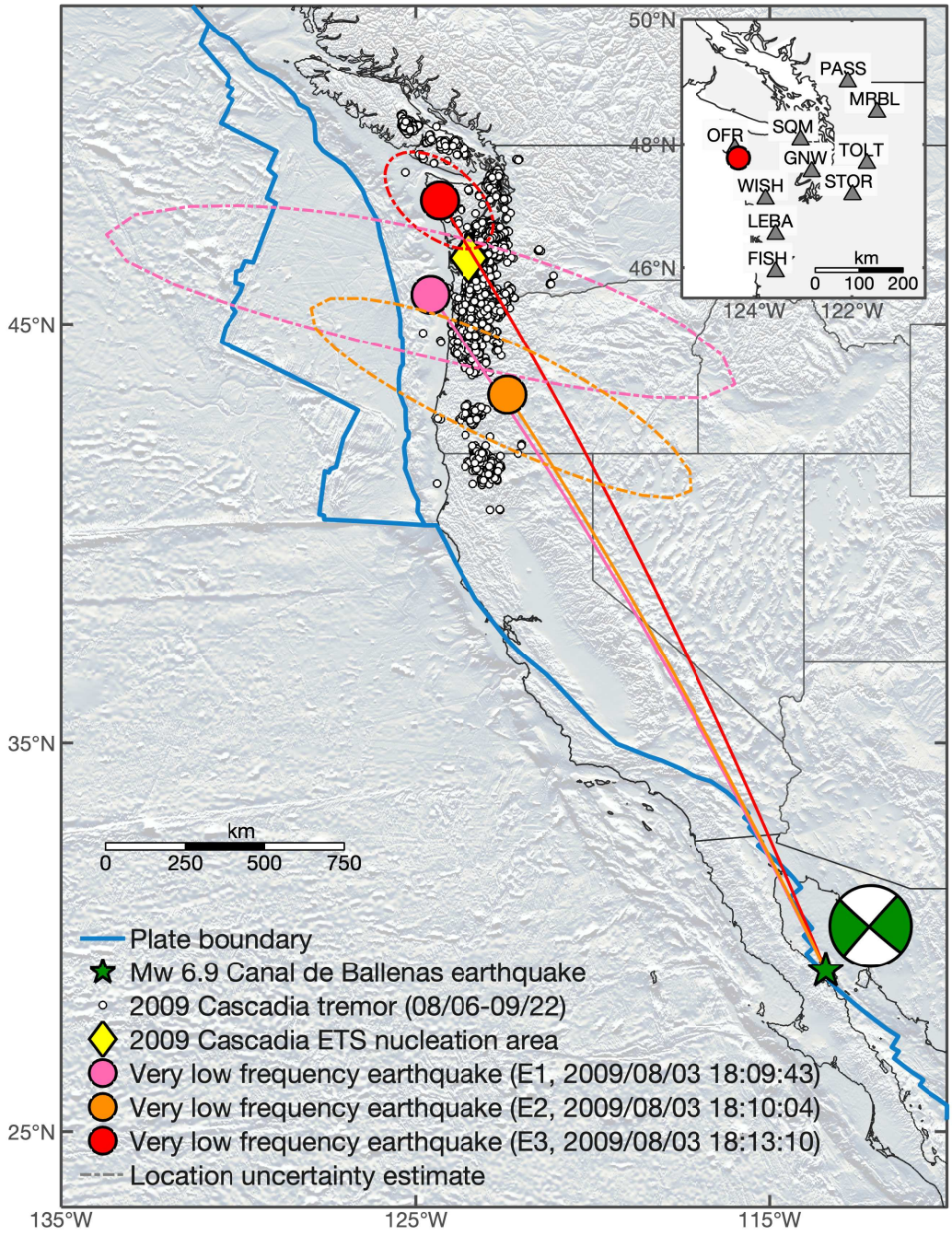

Figure 1. The 2009 M6.9 Canal de Ballenas earthquake, the 2009 Cascadia episodic tremor and slip (ETS) event, and three dynamically triggered very low frequency earthquakes (VLFEs, E1–E3). The tremor catalog is from the Pacific Northwest Seismic Network (PNSN). Inset: broadband near-field stations in the Pacific Northwest.

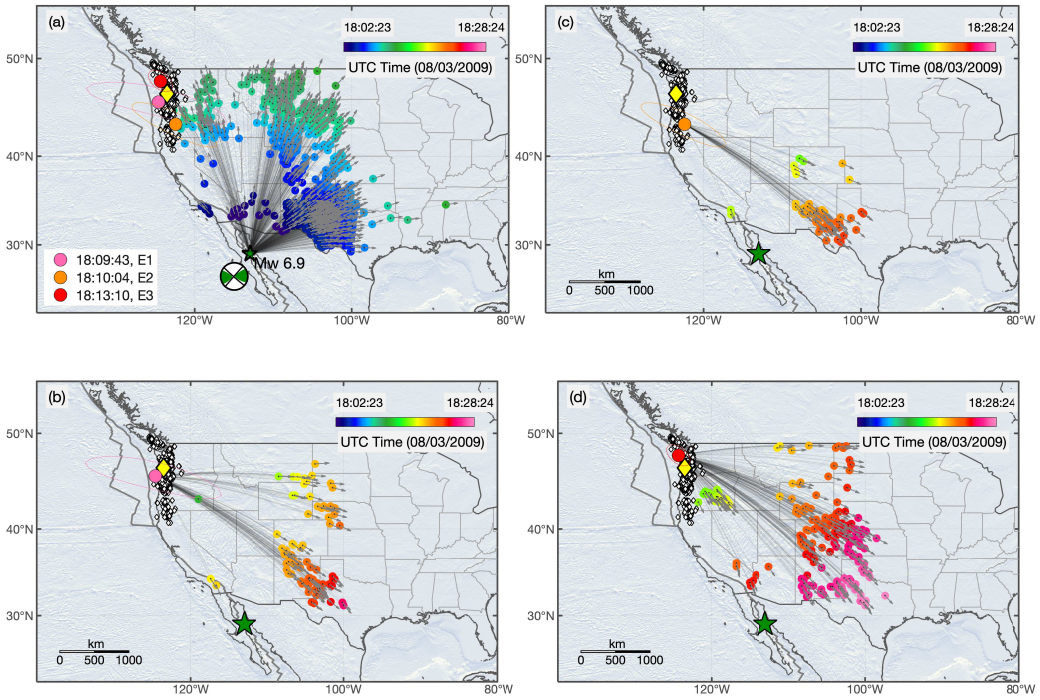

Figure 2. The very low frequency earthquakes and the triggering 2009 M6.9 earthquake (a). The legends are similar to those of Figure 1. The Rayleigh wave arrival times and propagation directions are shown as the colored dots and arrows. The thin gray lines show the great circle paths from the source to the subarrays. The four events share the same colorbar. These three VLFEs were detected and located by 84 subarrays at 45.67°/−124.58° (b), by 57 subarrays at 43.37°/−122.41° (c), and by 187 subarrays at 47.78°/−124.32°(d).

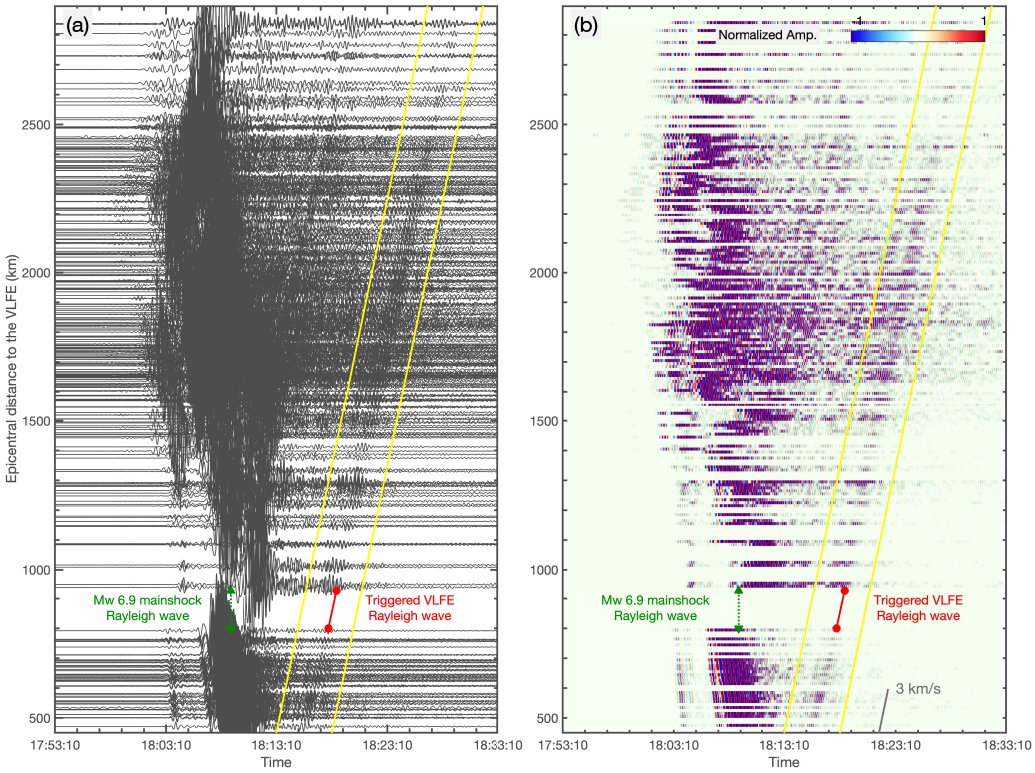

Figure 3. Record sections that are aligned with the epicenter of the VLFE E3 in Figure 2d. The records are self-normalized and bandpass-filtered to show signals in the 20–50 s period band. The yellow lines show a 3 km/s reference move-out velocity, windowing the VLFE waveforms. (a), waveform records. (b), polarity plot of the records that red color indicates positive polarity while blue color indicates negative polarity. Coherent phases can be easily identified by tracing coherent polarities.

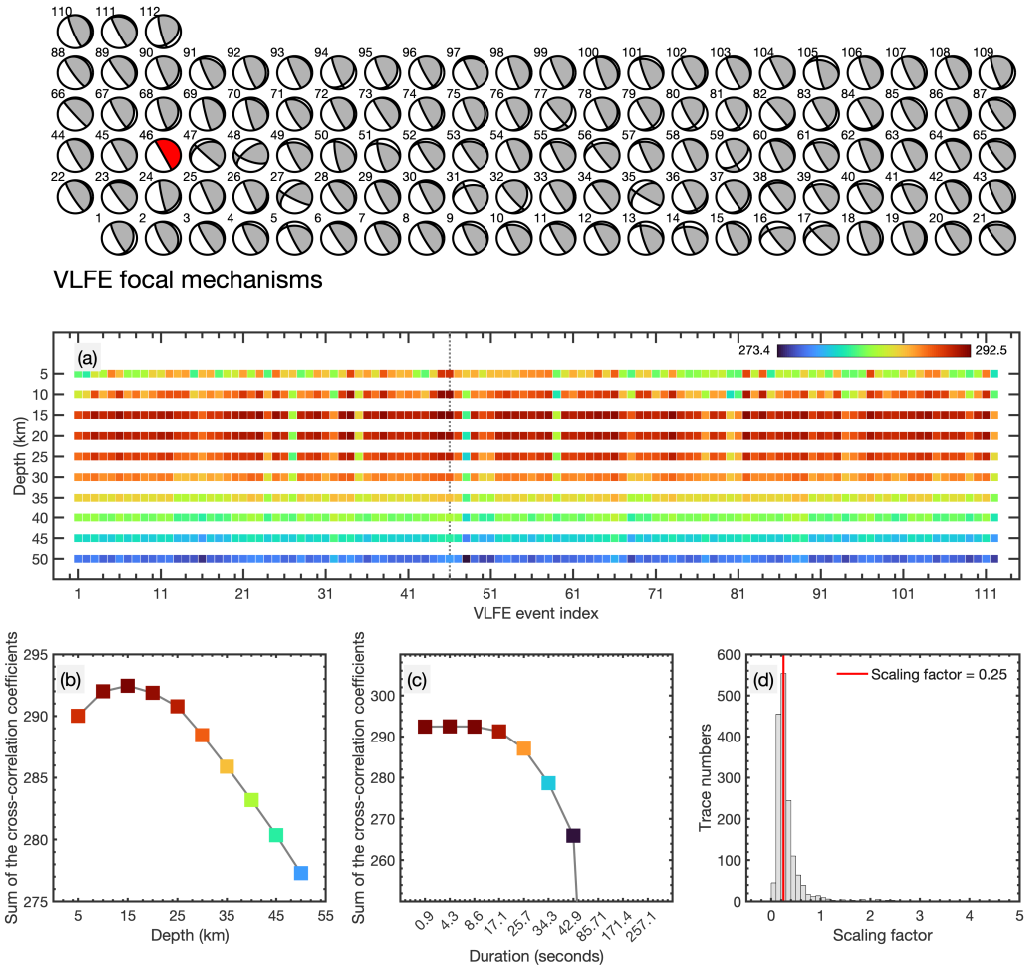

Figure 4. Determining the focal mechanism of VLFE E3. The VLFE focal mechanisms are shown in the top panel with their event index listed at their upper left corner [*Ide*, 2016]. The optimal focal mechanism is denoted as the red beachball. (a), total cross-correlation coefficients of the 112 candidate focal mechanisms. The total cross-correlation coefficient for a focal mechanism is the sum of the average cross-correlation coefficients of all the analyzed stations. (b), VLFE depth of E3 event showing total cross-correlation coefficients for the optimal focal mechanism at depth from 5 to 50 km (c), VLFE duration of E3 showing total cross-correlation coefficients for the optimal focal mechanism with duration from 0.9 to 257.1 seconds. We assume a Gaussian function shape with the duration as 6 times the standard deviation.(d) scaling factor of the VLFE moment. The testing moment is 2×10^{18} N $\cdot$ m. With the scaling factor, the VLFE moment is 0.5×10^{18} N $\cdot$ m, equivalent to a moment magnitude of 5.7.

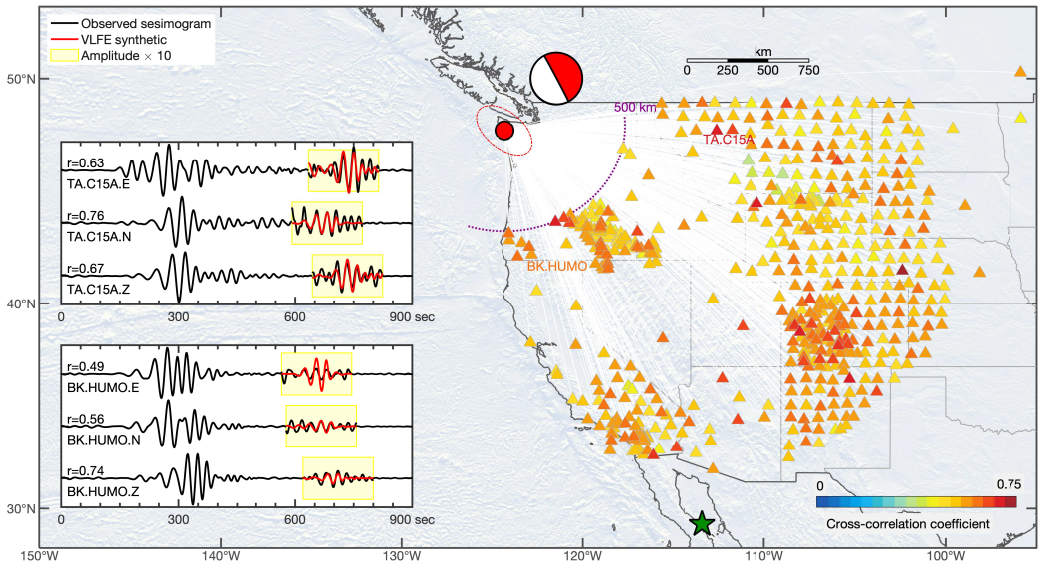

Figure 5. Seismic observations of E3 showing the average cross-correlation coefficients of the synthetic and observed waveforms of the VLFE E3. The average cross-correlation coefficient of a station is obtained by geometrically averaging coefficients of the three-component records. The legends are similar to those in Figure 1. The green star shows the 2009 M6.9 Canal de Ballenas earthquake. The red circle is VLFE E3. The beachball focal mechanism shows the preferred solution for VLFE E3. Triangles show seismic stations with their colors corresponding to the average cross-correlation coefficients. Waveforms of two annotated stations, TA.C15A and BK.HUMO, are shown in the insets. Insets: example three-component waveforms of the main-shock and the VLFE, overlain with synthetic waveforms of the VLFE. The two stations are at the eastward and the southward directions of the VLFE, respectively. The yellow shaded regions show records amplified by ten times.

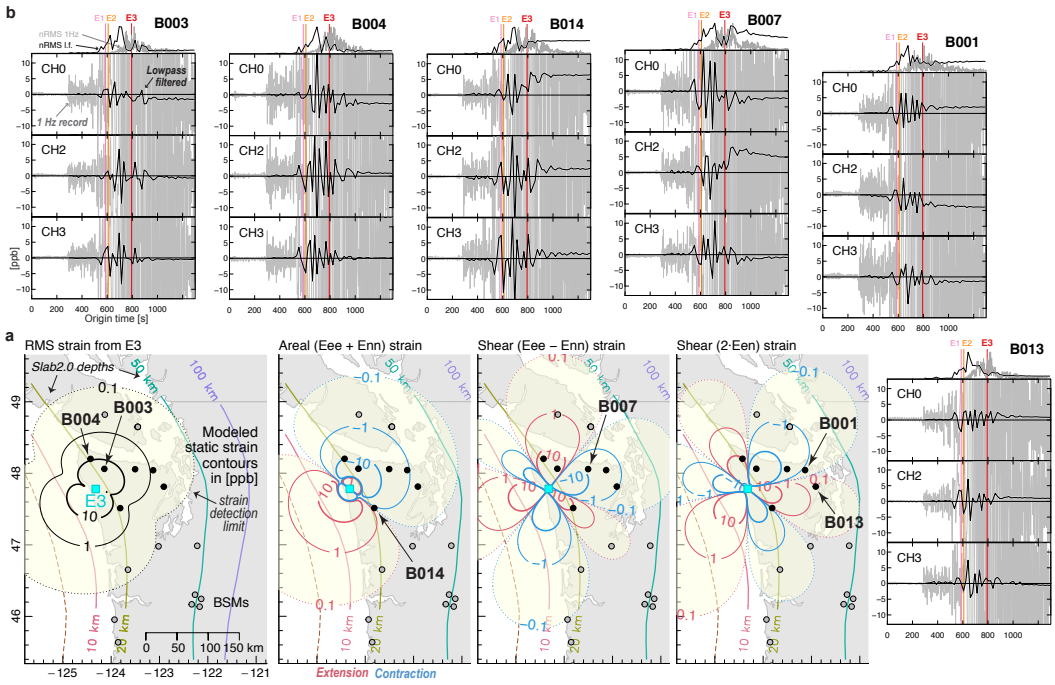

Figure 6. Static strains associated with triggered VLFE detection E3. (a) Contours of modeled static deformation from the best fitting focal mechanism for E3 (5), including root-mean-square (RMS) strain, areal strain (E_{ee} + E_{nn}), and the two engineering shear strains E_{ee} - E_{nn} and $2E_{en}$. Contours are limited to the theoretical strain detection limit of ~0.1 ppb. Stations in (b) are shown as filled circles. (b) Observations of static strains in high-frequency (1 Hz) strain records from B003, B004, B014, B007, B001, and B013. For each strain channel, we show the lowpass filtered record, obtained with a causal filter with a 18 s corner period (56 mHz), overlain on the original record. (Note that the 1 Hz records are not clipped; rather, the vertical scales are set to highlight signals in the low pass filtered record.) Vertical lines show the origin times of the VLFE detections E1–E3: static strains are not apparent until after E3. Self-normalized RMS strain records are shown at the top: E3 occurs around the time of maximum 1 Hz RMS strain (grey), after the peak in low-frequency RMS strain (black).

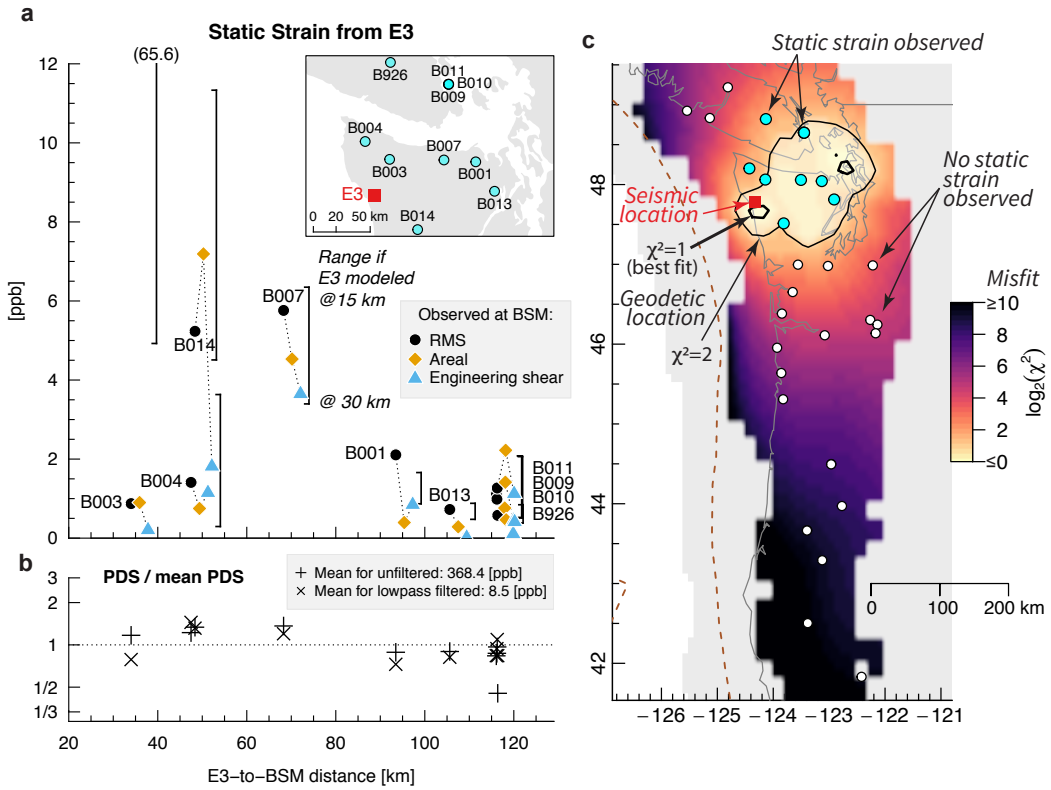

Figure 7. Observed static strains compared to variability in modeled strain due to depth and location uncertainty. (a) Observed tensor strains and the range of model results found by fixing the source epicenter but varying the source depth from 15 km to 30 km. (b) Peak dynamic strains (PDS) from the teleseimic waves. Points show the ratio of the PDS at each station to the mean value for all stations, for both unfiltered (1 Hz) and lowpassed (56 mHz) records; values are shown on a log scale. As expected, the PDS is relatively consistent across the study region. (c) Map of source likelihood found by moving the E3 source to each point on the Slab2.0 depth surface [i.e., *Hayes et al.*, 2018], forward modeling the static strains, and computing the misfit. Colors show the base-2 logarithm of the reduced Chi-squared misfit (χ^2); the thick black line shows the region where residual variance is equal to observational variance ($\chi^2 = 1$). There are two small regions of lowest-misfit; one is near the location of E3 determined independently with seismic data.

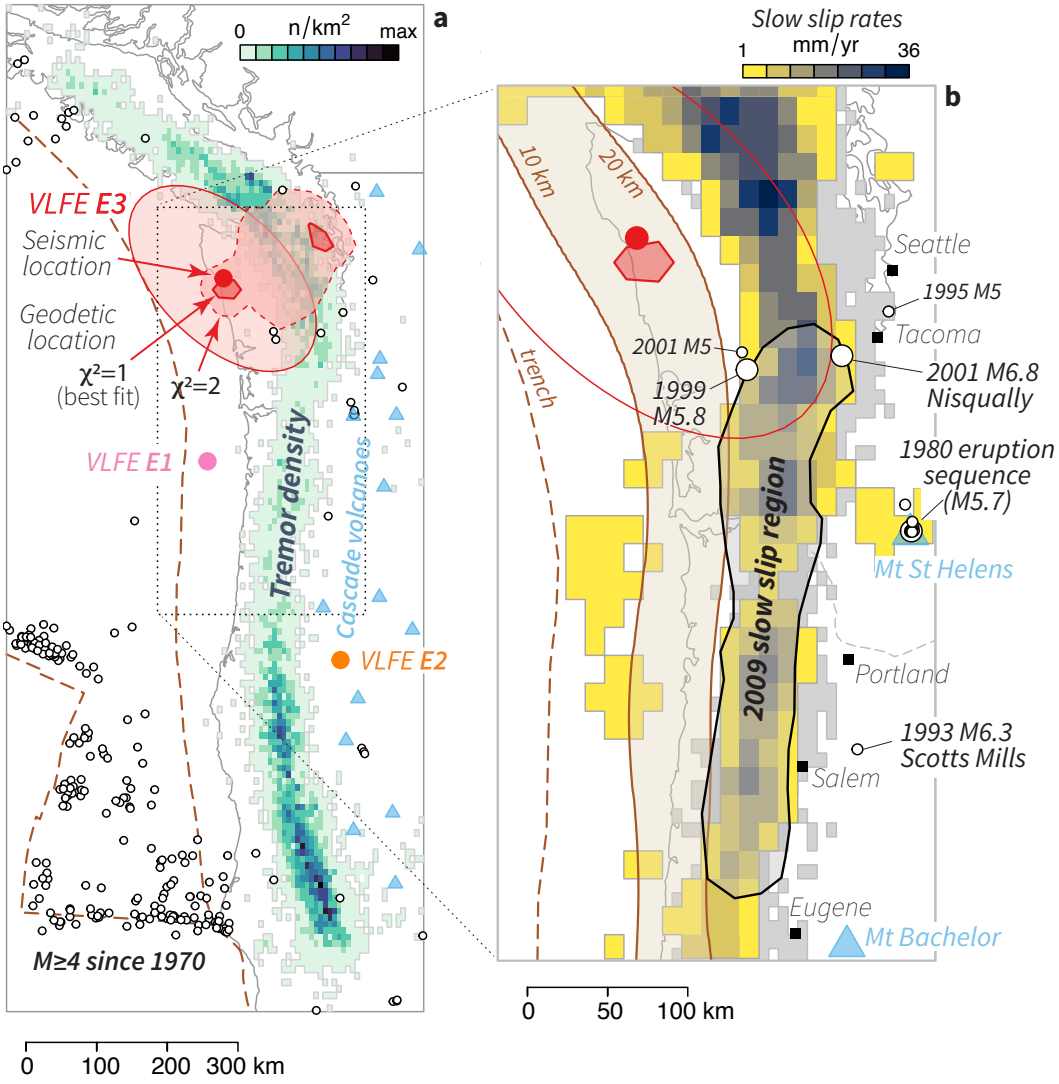

Figure 8. VLFE E3 in the seismogenic transition zone. (a) Locations of VLFEs E1–E3, seismic and geodetic location uncertainties for E3, tectonic tremor densities [e.g., *Wech and Creager*, 2008], and crustal seismicity with M≥4, since 1970 [e.g., *U.S. Geological Survey*, 2017]. (b) Zoom in map of the location of E3, which both seismic and geodetic data indicate is between the 10 and 20 km depth contours according to the Slab2.0 model [i.e., *Hayes et al.*, 2018]. This is outside of the tectonic tremor region [grey area, from (a)], the 2009 slow slip region [*Bartlow et al.*, 2011], and the region where average slow slip rates are resolvable at >1 mm/yr levels [*Bartlow*, 2020].

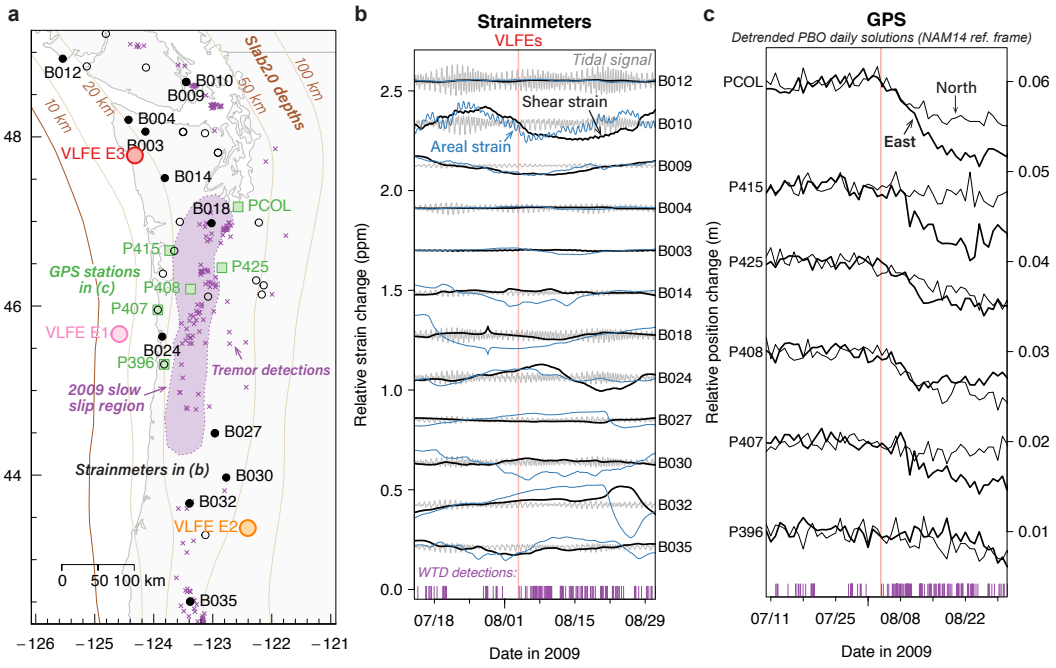

Figure 9. Timing of VLFEs compared to the 2009 slow slip event. (a) Map of the VLFEs, the slow slip region [*Bartlow et al.*, 2011] and the primary GPS stations used to constrain the slip patch, tremor detections from the World Tremor Database (WTD) [*Idehara et al.*, 2014], and the NOTA BSM network (circles). (b) Shear and areal strains from the NOTA strainmeters highlighed in (a), from 2009/7/12 to 2009/9/1. Strains have been corrected for atmospheric pressure and tides, detrended, and lowpass filtered with a causal filter with a corner period of 2.5 days. Shown below these timeseries is the WTD catalog (see a); the first event on 2009/8/3 occurred at 21:24:14 UTC, approximately 10 hours after the VLFEs. (c) Detrended timeseries of daily GPS positions at the stations shown in (a) during the same period. Noise levels notwithstanding, the initiation of the 2009 ETS slow slip event appears to coincide with the VLFEs; slip is modeled to begin after 8/3 and is clearly developed by the 7th [*Bartlow et al.*, 2011].

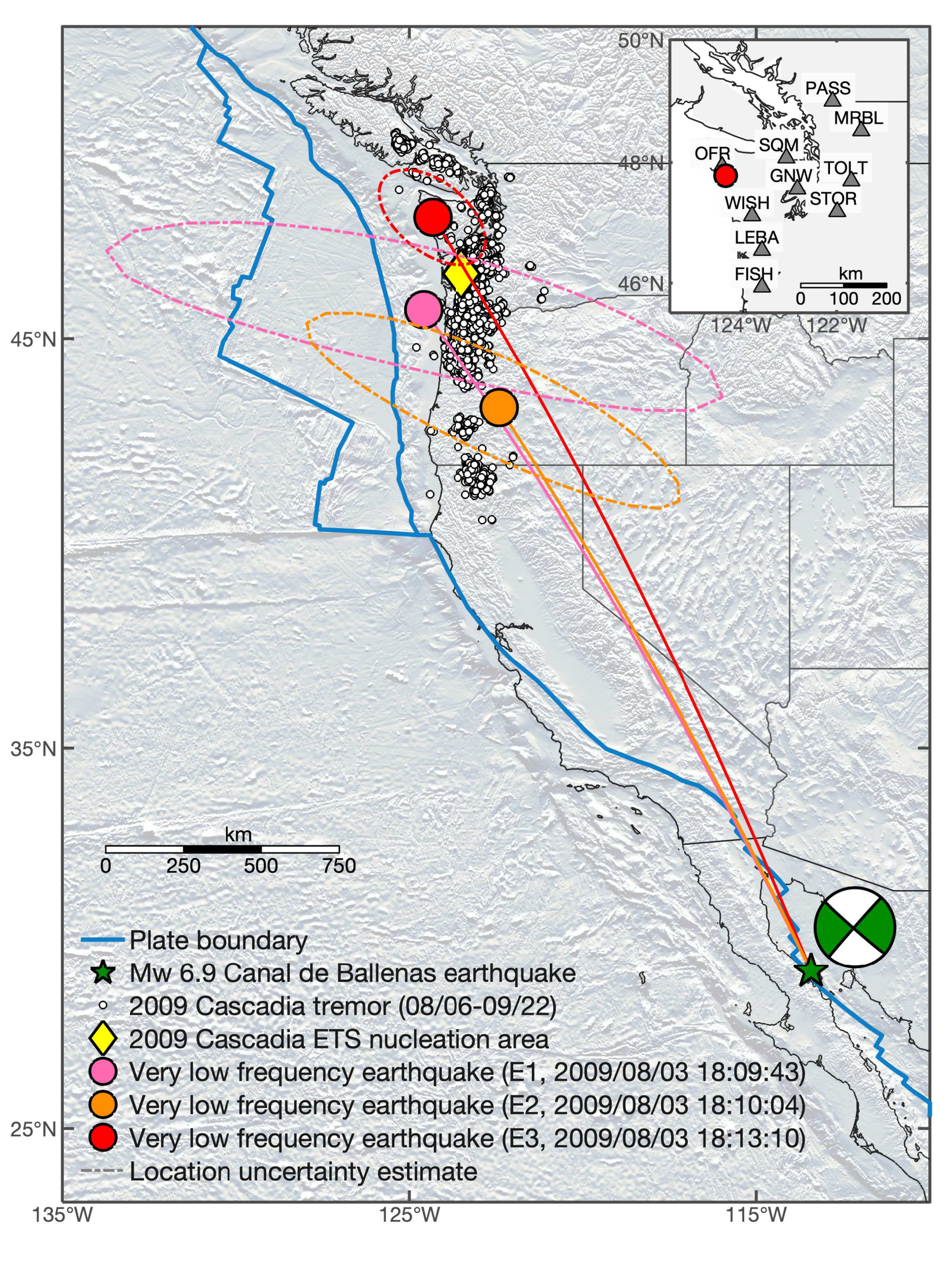
50°N
48°N
46°N
45°N
35°N
25°N
135°W
125°W
115°W
124°W
122°W
PASS
MRBL
SQM
OFR
GNW
TOLT
WISH
STOR
LEBA
FISH
km
0 100 200
km
0 250 500 750
Plate boundary
Mw 6.9 Canal de Ballenas earthquake
2009 Cascadia tremor (08/06-09/22)
2009 Cascadia ETS nucleation area
Very low frequency earthquake (E1, 2009/08/03 18:09:43)
Very low frequency earthquake (E2, 2009/08/03 18:10:04)
Very low frequency earthquake (E3, 2009/08/03 18:13:10)
Location uncertainty estimate

(a)

18:02:23 18:28:24

UTC Time (08/03/2009)

18:09:43, E1
18:10:04, E2
18:13:10, E3

Mw 6.9

50°N
40°N
30°N
120°W
100°W
80°W

(c)

18:02:23 18:28:24

UTC Time (08/03/2009)

50°N
40°N
30°N

km
0 500 1000

120°W
100°W
80°W

(b)

18:02:23 18:28:24

UTC Time (08/03/2009)

50°N
40°N
30°N

km
0 500 1000

120°W
100°W
80°W

(d)

18:02:23 18:28:24

UTC Time (08/03/2009)

50°N
40°N
30°N

km
0 500 1000

120°W
100°W
80°W

(a)

(b)

Normalized Amp.

−1

1

2500

2000

1500

1000

500

Epicentral distance to the VLFE (km)

Mw 6.9 mainshock
Rayleigh wave

Triggered VLFE
Rayleigh wave

3 km/s

17:53:10

18:03:10

18:13:10

18:23:10

18:33:10

Time

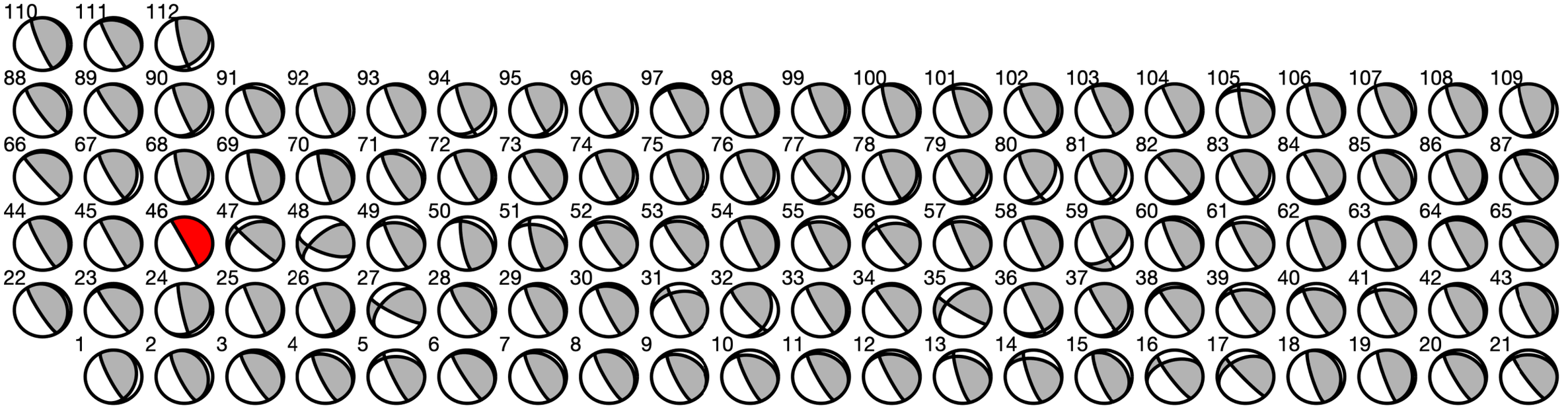

VLFE focal mechanisms

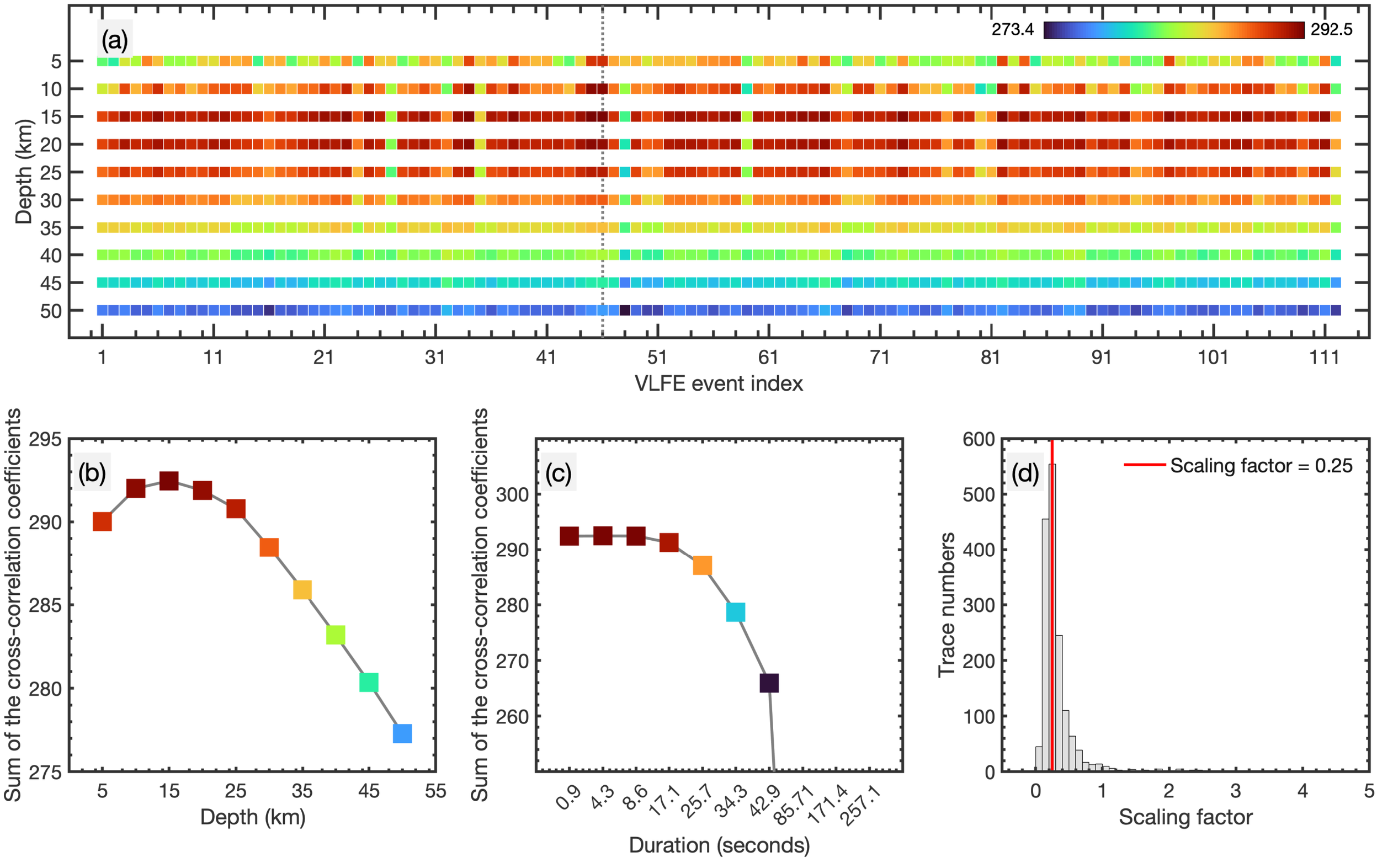

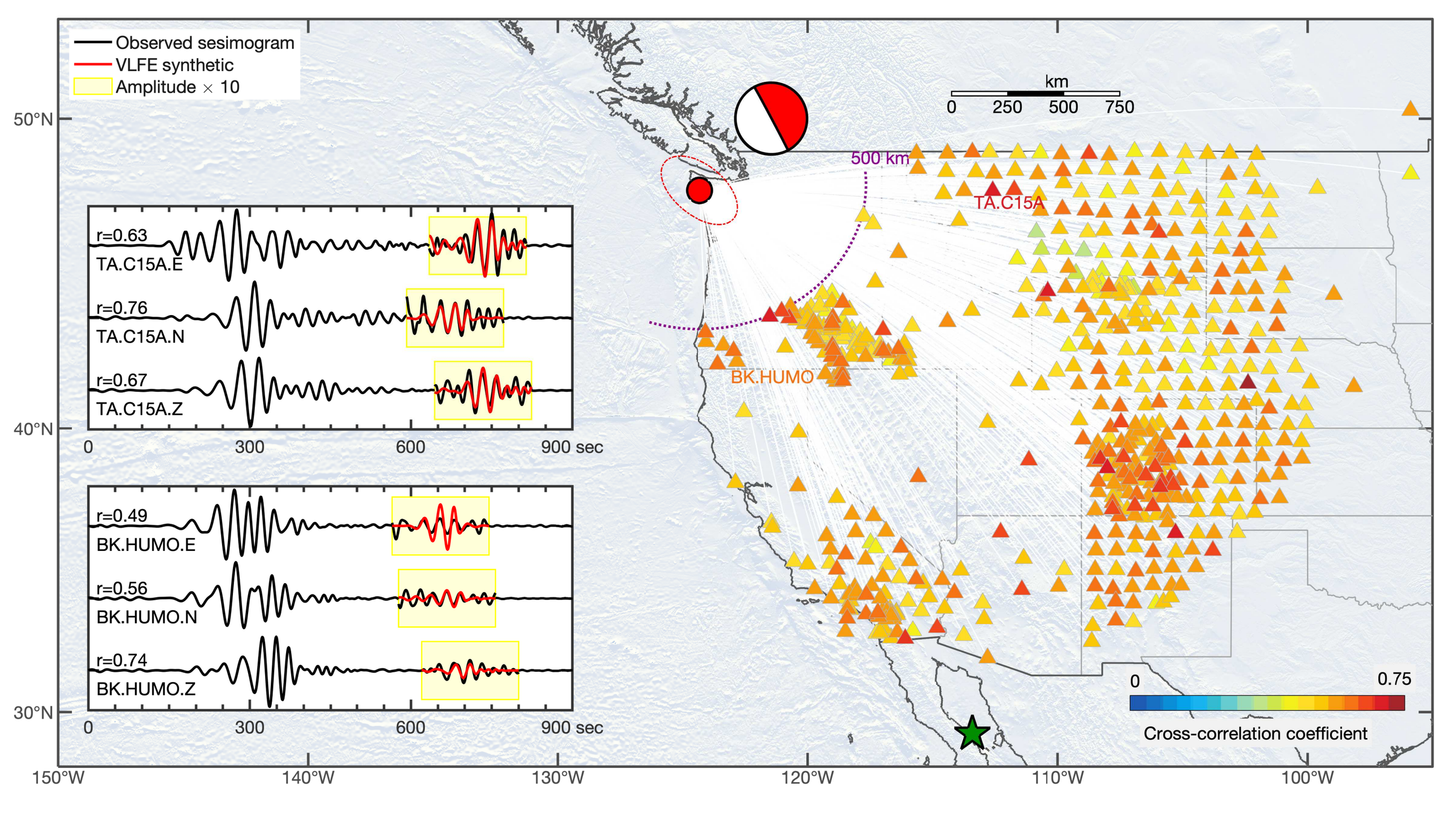
Observed sesimogram
VLFE synthetic
Amplitude × 10
km
0
250
500
750
500 km
TA.C15A
BK.HUMO
r=0.63
TA.C15A.E
r=0.76
TA.C15A.N
r=0.67
TA.C15A.Z
0
300
600
900 sec
r=0.49
BK.HUMO.E
r=0.56
BK.HUMO.N
r=0.74
BK.HUMO.Z
0
300
600
900 sec
0
0.75
Cross-correlation coefficient
50°N
40°N
30°N
150°W
140°W
130°W
120°W
110°W
100°W

b

B003 B004 B014 B007 B001

E1 E2 E3

nRMS 1Hz

nRMS l.f.

CH0 CH2 CH3

Lowpass filtered

1 Hz record

[ppb]

Origin time [s]

a

RMS strain from E3

Areal (Eee + Enn) strain

Shear (Eee – Enn) strain

Shear (2·Een) strain

Slab2.0 depths

50 km

100 km

Modeled static strain contours in [ppb]

strain detection limit

BSMs

E3

10 km

20 km

0 50 100 150 km

Extension Contraction

B013

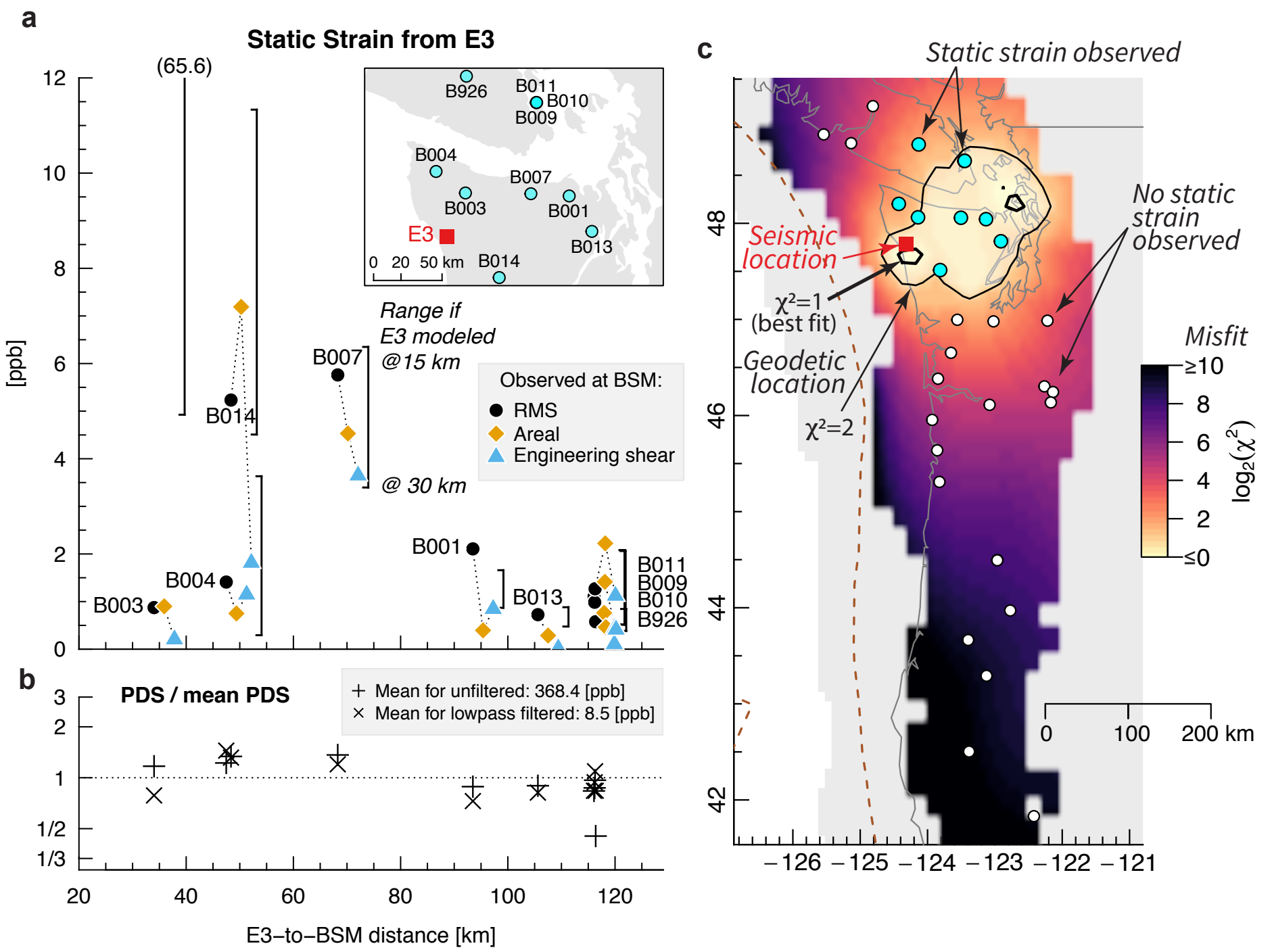
a
Static Strain from E3
(65.6)
B926
B011
B010
B009
B004
B007
B003
B001
E3
B013
0 20 50 km
B014
Range if
E3 modeled
@15 km
@ 30 km
Observed at BSM:
RMS
Areal
Engineering shear
[ppb]
B014
B007
B001
B004
B003
B013
B011
B009
B010
B926
b
PDS / mean PDS
Mean for unfiltered: 368.4 [ppb]
Mean for lowpass filtered: 8.5 [ppb]
E3–to–BSM distance [km]
c
Static strain observed
No static
strain
observed
Seismic
location
χ²=1
(best fit)
Geodetic
location
χ²=2
Misfit
log₂(χ²)
≥10
8
6
4
2
≤0
0 100 200 km

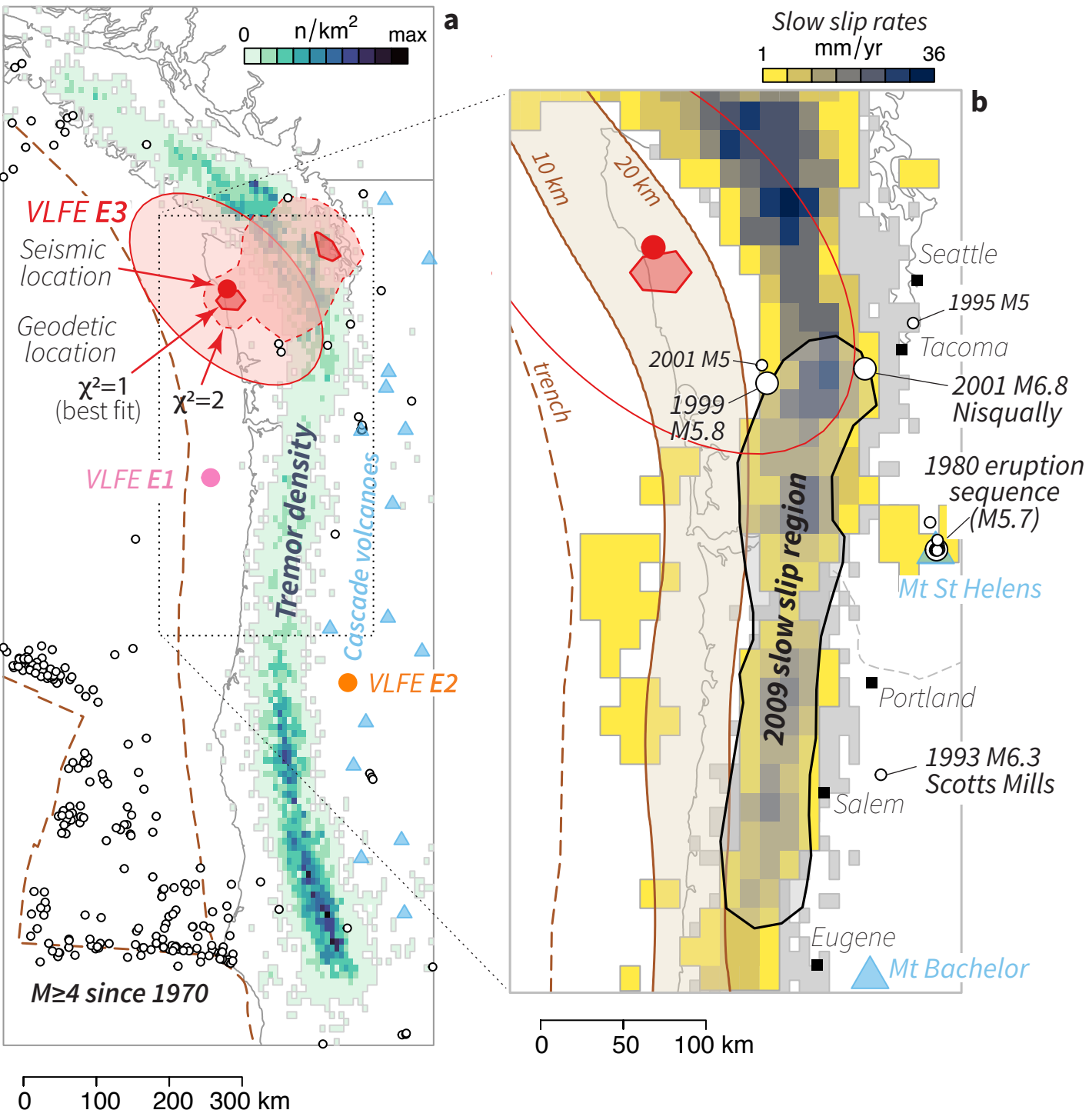
a
0
n/km²
max
VLFE E3
Seismic location
Geodetic location
χ²=1
(best fit)
χ²=2
VLFE E1
Tremor density
Cascade volcanoes
VLFE E2
M≥4 since 1970
0
100
200
300 km
Slow slip rates
1
mm/yr
36
b
10 km
20 km
trench
2001 M5
1999 M5.8
2009 slow slip region
Seattle
1995 M5
Tacoma
2001 M6.8 Nisqually
1980 eruption sequence (M5.7)
Mt St Helens
Portland
1993 M6.3 Scotts Mills
Salem
Eugene
Mt Bachelor
0
50
100 km

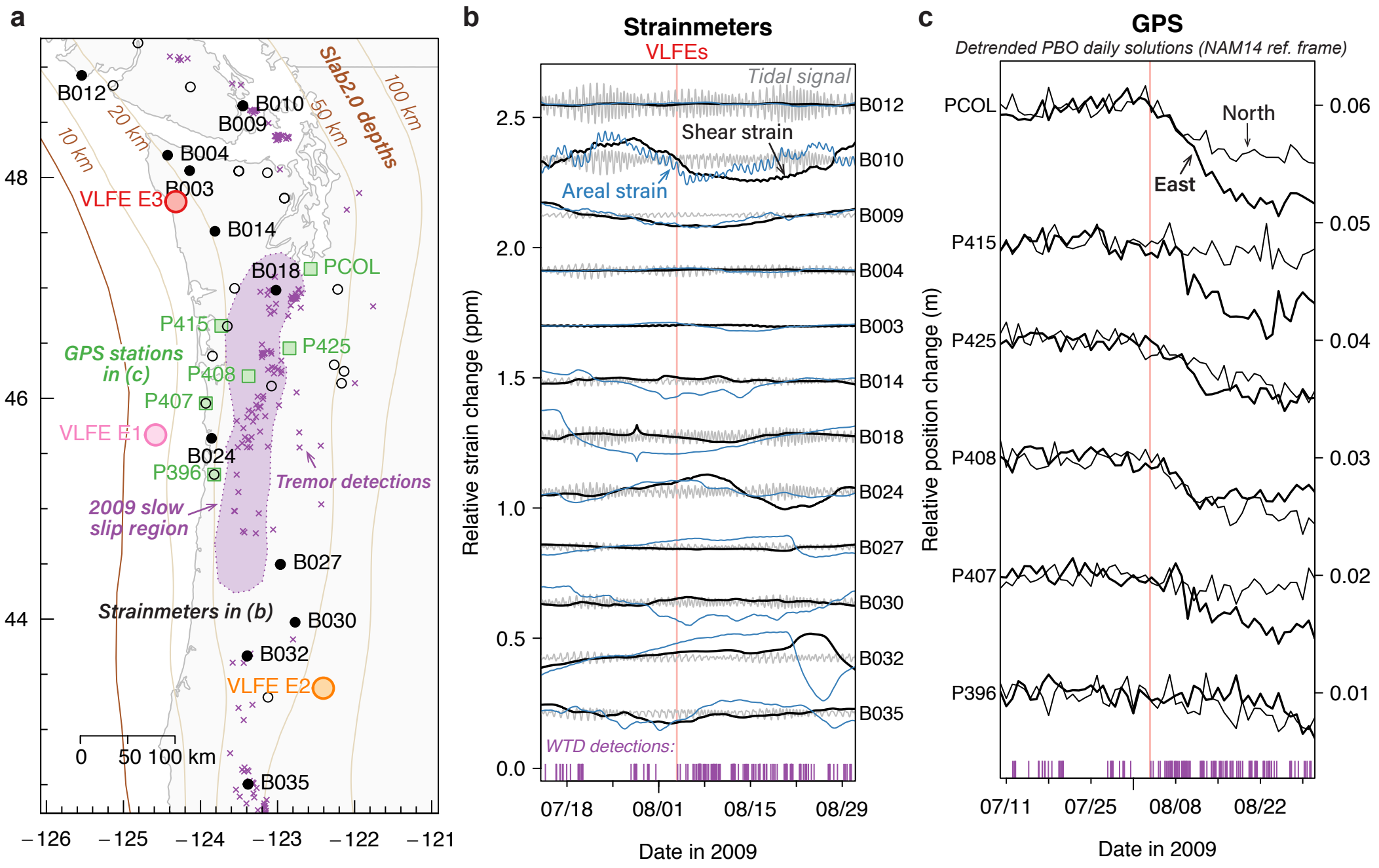
a
b
c
Slab2.0 depths
10 km
20 km
50 km
100 km
B012
B010
B009
B004
B003
VLFE E3
B014
B018
PCOL
P415
P425
GPS stations in (c)
P408
P407
VLFE E1
B024
P396
Tremor detections
2009 slow slip region
B027
Strainmeters in (b)
B030
B032
VLFE E2
B035
0 50 100 km
48
46
44
−126 −125 −124 −123 −122 −121
Strainmeters
VLFEs
Tidal signal
Shear strain
Areal strain
Relative strain change (ppm)
2.5
2.0
1.5
1.0
0.5
0.0
B012
B010
B009
B004
B003
B014
B018
B024
B027
B030
B032
B035
WTD detections:
07/18
08/01
08/15
08/29
Date in 2009
GPS
Detrended PBO daily solutions (NAM14 ref. frame)
North
East
PCOL
P415
P425
P408
P407
P396
Relative position change (m)
0.06
0.05
0.04
0.03
0.02
0.01
07/11
07/25
08/08
08/22
Date in 2009